Int J Fract (2017) 206:95–122
DOI 10.1007/s10704-017-0203-5

ORIGINAL PAPER

Interaction of the Portevin–Le Chatelier phenomenon with ductile fracture of a thin aluminum CT specimen: experiments and simulations

Gilles Rousselier · Thilo F. Morgeneyer · Sicong Ren · Matthieu Mazière · Samuel Forest

Received: 1 December 2016 / Accepted: 7 March 2017 / Published online: 17 March 2017

Abstract An attempt is made here to capture numerically slant ductile fracture and its early slant strain precursors via combining a dynamic strain aging (DSA) model with ductile damage models. In recent experimental studies it has been shown that in an AA2XXX alloy strain localization in slant bands preceded the onset of damage, originating slant fracture ahead of a notch. Here tensile tests are performed at different strain rates revealing some negative strain rate sensitivity which is an indication of DSA effect for AA2198-T8. A McCormick-type DSA model in conjunction with a Rousselier damage model, a reduced polycrystalline plasticity model and a Coulomb fracture criterion for slip systems have been used. Full 3D finite element simulations using this model and typical parameters for aluminum alloys capture the early strain localization in slanted bands, their intermittent activity and the final slant fracture. Prior simulation results without the DSA model and others using the von Mises plasticity or the GTN model did not capture the early slant strain localization thereby suggesting that DSA may well be the physical origin of the early slant strain localization and final slant fracture phenomena in this alloy.

G. Rousselier (✉) · T. F. Morgeneyer · S. Ren · M. Mazière · S. Forest
MINES ParisTech, MAT - Centre des Matériaux, CNRS UMR 7633, PSL Research University, BP 87, 91003 Evry Cedex, France
e-mail: gilles.rousselier@mines-paristech.fr

Keywords Aluminum alloy · Dynamic strain aging · Finite elements · Fracture mechanisms · Polycrystalline model · Synchrotron laminography

1 Introduction

The understanding and prediction of strain and damage interactions in ductile alloys remain a crucial topic e.g. due to the need for weight reduction without compromising passenger safety in transport applications. The development of novel alloys and enhanced joining techniques (Le Jolu et al. 2014, 2015) make ductile alloy candidates for future structural applications. This understanding of strain and damage interactions is important for micromechanics-based development of new materials and the assessment of structural integrity.

Ductile fracture is commonly linked to ductile fracture micromechanisms which are: the nucleation of voids, their growth and final coalescence. However, failure in cases where strain localization takes place and also in cases where the triaxial stress, the driving force of void growth during ductile deformation, is low, i.e. typically below 1 (Papasidero et al. 2014) is poorly understood. An insufficiently understood phenomenon linked to localization and strain and damage interactions during ductile tearing is slant fracture (Mahgoub et al. 2003).

With recent advances in synchrotron imaging (Maire et al. 2011; Maire and Withers 2014) and strain measurement techniques via digital volume correlation

(Morgeneyer et al. 2013), it has become possible to measure damage and strain evolution in situ and in three dimensions non-destructively. For the observation of damage and strain interaction during ductile tearing of sheet materials synchrotron laminography is particularly adapted (Helfen et al. 2012).

For an Al–Cu–Li alloy with low work hardening (AA2198-T8) it has been shown with these techniques that slant strained bands precede the onset of damage and the slant crack (Morgeneyer et al. 2014). This region of the sample has been shown to be in a plane strain state with respect to the crack propagation direction (Buljac et al. 2016). It has also been shown that the ratio between the strain in the band and outside of the band was of the order of 2 (Morgeneyer et al. 2014). In other words, the material outside the bands also deforms during every load step, except for the very last ones, but to a lesser extent than the material within the band. For the last load step deformation only occurs within the band. Strain concentrations in a slant band were observed very early on and the scene for localization and fracture was already set. For another 2XXX alloy with initial porosity and strong work hardening (AA2139-T3), the early strain localization in slanted bands ahead of a notch has been confirmed via the mentioned techniques (Morgeneyer et al. 2016). Intermittent band activity and their relative stability in space could be confirmed. Von Mises plasticity or a GTN-type model did not manage to reproduce the above mentioned findings in terms of slant bands or slant fracture (Morgeneyer et al. 2014).

Slant fracture is hard to reproduce numerically in general (Besson 2010). This could be linked to numerical problems due to mesh dependence of local models (Besson et al. 2001). Slant fracture has successfully been simulated using shear void nucleation based on the Lode parameter (Morgeneyer and Besson 2011) that actually resembles the shear modification of the Gurson model (Nahshon and Hutchinson 2008). In Morgeneyer et al. (2016), this model has been used. Slant fracture was reproduced successfully but the early strain localization could not be captured. In Besson et al. (2013) it has been shown via a computational cell simulation that the dissipated energy reaches a minimum when the crack is slanted. Experimentally, slant fracture is widely observed in thin walled structures (Pardoen and Hutchinson 2003) and can also lead to flip-flopping phenomena (El-Naaman and Nielsen 2013; Simonsen and Tornqvist 2004) that are neither understood nor reproduced numerically, although out-of-plane loading in thin sheets is a possible explanation.

One objective of the present work is to investigate whether the multiple and intermittent crossing strain bands could be related to dynamic strain aging (DSA) via simulations. In aluminum alloys at room temperature, DSA can also be involved in ductile fracture. Shear banding in aluminum alloys at room temperature has also been attributed to DSA and the Portevin–Le-Chatelier (PLC) effect (Le Chatelier 1909; Portevin and Le Chatelier 1923). It led to equally spaced rough bands on the surface of a Kahn tear test specimen made of Al–Li alloy (Delafosse et al. 1993). In Clausen et al. (2004), it was noted that shear failure only occurred inside the PLC domain. The macroscopic KEMC model has been used for DSA in many papers (Zhang et al. 2001; Graff et al. 2004; Benallal et al. 2008; Belotteau et al. 2009; Mazière et al. 2010; Wang et al. 2011). In the present paper, the polycrystalline framework enables to use this model at the slip system scale, which seems more appropriate (Rousselier and Quilici 2015; Marchenko et al. 2016). The limitation is numerical: for a fixed loading rate, the KEMC model is intrinsically unstable when the so-called waiting time $t_w = \omega/|\dot{\gamma}|$ decreases, where $\dot{\gamma}$ is the slip rate (or the strain rate in a macroscopic model) and ω is the strain parameter of the model. Very small time steps are then required to describe the transient behavior of PLC. Also, when the parameter ω is very small for a given loading rate, the numerical integration fails in some finite elements.

Another objective is to investigate the transition from flat to slant fracture in a thin aluminum CT specimen. In some aluminum alloys, fracture surfaces do not show the dimples related to void damage and another mechanism is involved, in particular in slant and shear fracture (Rousselier and Luo 2014; Morgeneyer et al. 2014). In Rousselier and Luo (2014), the Coulomb fracture model (Coulomb 1773) was combined with the Rousselier damage model in the framework of polycrystalline plasticity. In the present work, the combination of these models with the KEMC model enables to investigate the interactions of DSA with ductile fracture. The combination of all the above-mentioned models is required to match the whole set of experimental measurements and observations. It leads to several difficulties and the calculations are at the limit of what is reasonably achievable. In finite element (FE) analyses, the CPU time is very long because of the small time steps required by the DSA model. For most of

the calculations, a relatively coarse finite element mesh is used to limit the CPU time. Another difficulty is the mesh dependence in fracture predictions, in particular the propagation of a slant crack in a Cartesian mesh for which a pragmatic method is used. The modeling choices can be discussed but they succeeded in reproducing qualitatively and quantitatively the localized strain pattern found experimentally and the main features of physical damage and of flat to slant fracture transition.

The paper is structured as follows: material data and experimental results from tensile tests are given to assess the PLC effect for the material. Experimental findings for strain and damage interaction during tearing measured by laminography and digital volume correlation (DVC) are recalled. Fracture mechanisms are discussed. The combined models are presented and the material parameters are calibrated with the existing observations and data. The numerical strain patterns are compared to the measured ones. The flat to slant fracture transition is shown for coarse and fine meshes. The achievements and limitations of the current work are then discussed and the main conclusions are drawn.

2 Experimental results for AA2198-T8R

2.1 Material

The 2.0 mm thick aluminum sheet was provided by Constellium in the recrystallized state and after an artificial ageing treatment (T8) generating nanometric hardening precipitates. The composition is 2.9–3.5Cu, 0.8–1.1Li, 0.25–0.8Mg, 0.1–0.5Ag, 0.04–0.18Zr (in wt.%), balance Al. The intermetallic particles volume fraction is ∼0.3–0.4%, their size is 2–3 μm. Almost no initial porosity was found (<0.03 vol%). The grains are elongated to ∼200–300 μm in the longitudinal L direction and to ∼60 μm in the transverse T direction. The typical grain size in the short transverse S direction is ∼25–30 μm. The yield strength is ∼440 MPa and the ultimate tensile strength is ∼500 MPa, showing relatively low work hardening. The material has moderate texture and hardly any anisotropy measured in stress–strain curves.

The room temperature experimental tensile curves in the transverse direction are plotted in Fig. 1, using the nominal strain measured by the extensometer (ΔL: elongation, L0: extensometer gage length = 25 mm, specimen width = 6 mm, thickness = 2 mm). A small but significant negative strain rate sensitivity equal to 4 MPa is observed in this alloy between 10^{-4} and $10^{-2}\,s^{-1}$. Repeated tests at the same strain rate give a scatter smaller than 1 MPa. Serrations are larger for $10^{-2}\,s^{-1}$ in the enlargement of Fig. 1b, but they also appear in other regions of the curves in Fig. 1a. As the PLC effect is sensitive to temperature and strain rate, the current test conditions seem to be located around the lower boundary of the PLC sensitive zone (see Fig. 3 in Lebyodkin et al. 2000).

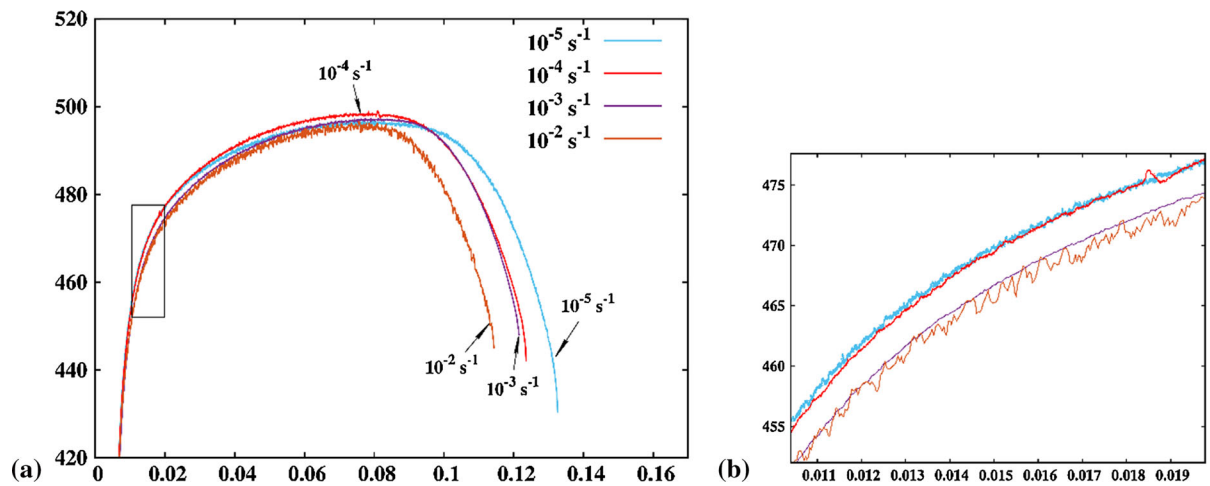

Fig. 1 Tensile curves in T-direction, elongation rates 10^{-5} to $10^{-2}\,s^{-1}$, F/S0 (MPa) versus Δ L/L0: **a** 420–520 MPa range and **b** 450–480 MPa range

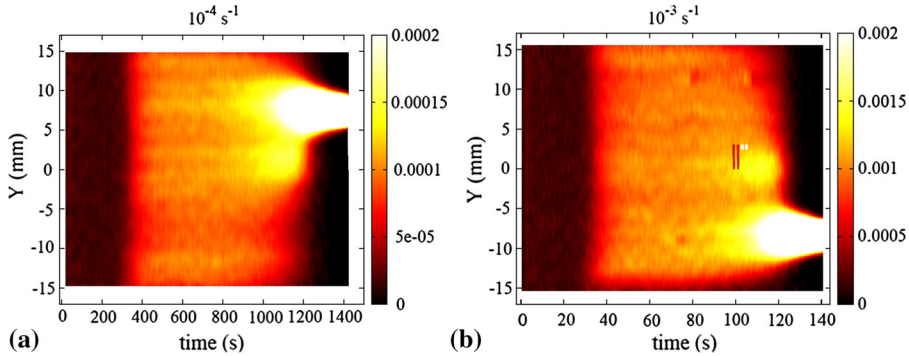

Fig. 2 Tensile tests in T-direction, strain rate (s^{-1}) along the specimen gage length (coordinate Y) versus time (s), elongation rates: **a** 10^{-4} s^{-1}, noise $\sim 10^{-5}$ s^{-1}, **b** 10^{-3} s^{-1}, noise $\sim 10^{-4}$ s^{-1}. The strain rate scale is on the *right of each figure*

The strain rate measured by 2D digital image correlation (DIC) on the specimen surface is non-homogeneous in the gauge length. It can be seen in the space–time figures for 10^{-4} and 10^{-3} s^{-1} (Fig. 2: in this figure, the strain along a line in the specimen length direction Y is plotted vs. time). The tests at 10^{-2} s^{-1} show the same features. The heterogeneities are significantly larger than the estimated measurement noise, equal approximately to 10^{-5} and 10^{-4} s^{-1} in Fig. 2a, b, respectively. They have more or less fixed locations. For 10^{-3} s^{-1}, the locations are more mobile. The characteristic length of the heterogeneities is larger than $\sim$1 mm. In this 2198-T8R alloy, DIC does not reveal the mobile inclined strain rate bands that can be seen for example in 2198-T3R with the same chemical composition but with a different heat treatment. For nominal strains $\Delta L/L0$ larger than 0.1, the strain rate concentrates in some fixed regions of the gauge length and eventually in a fixed horizontal band corresponding to through-the-thickness slant fracture.

2.2 Laminography (CT specimen)

A CT-like specimen with dimensions: width W = 60 mm, height H = 70 mm, thickness B = 1 mm, notch length a = 36 mm, ligament W − a = 24 mm, notch radius $\rho = 0.17$ mm, was investigated by in situ X-ray laminography at the European Synchrotron Radiation Facility (ESRF, Grenoble, France) (Morgeneyer et al. 2014). A schematic view of the laminography experimental set-up is shown in Fig. 3a. An anti-buckling device was used to limit out-of-plane displacements. A 3-D reconstructed volume of the notch region in the initial unloaded state is also shown in Fig. 3a. The gray levels give the notch geometry, the voids and the cracks in plane sections and in reconstructed volumes. The specimen is loaded in the T–L configuration. The coordinates x, y, z correspond to L, T, S, respectively. The two regions of interest (ROI 1 and ROI 2) defined in Fig. 3b were analyzed with digital volume correlation (DVC). Sections normal to L and S-axes are referred to as L and S-sections in the sequel. The results are presented and discussed in Morgeneyer et al. (2014) and Buljac et al. (2016).

A stepwise loading was applied on the crack with screws (Fig. 3a). Each loading step is applied within several seconds. The displacement is kept constant during the laminography scans. More details are given in Morgeneyer et al. (2014). The notch opening was measured at a mid-thickness point in the notch $\sim$200 μm in front of the initial notch tip using the laminography images (e.g. Fig. 3). The notch opening *displacement* (NOD) is obtained by subtracting the initial notch opening (Table 1). The time is the one of the FE calculations; it is defined in Sect. 4.3.

2.3 Strain fields

Figure 4a shows the *incremental* equivalent strain fields in the ROI 1 for the previously described loading steps: 1–2, 2–3 and 3–4 (the correlation quality was insufficient for step 5). The incremental activity of the localization bands can be seen more clearly in this representation than for the *total* equivalent strain fields. (Incremental strain fields calculated by FE analysis are shown for comparison. The used model combines a Rousselier damage model with dynamic strain aging, a reduced polycrystalline model and a Coulomb model at the slip system scale for damage. The model and the simulations are discussed in Sect. 4.4.) For steps 1–2, the main experimentally measured band is approximately oriented at minus 45° in the yz plane and several parallel

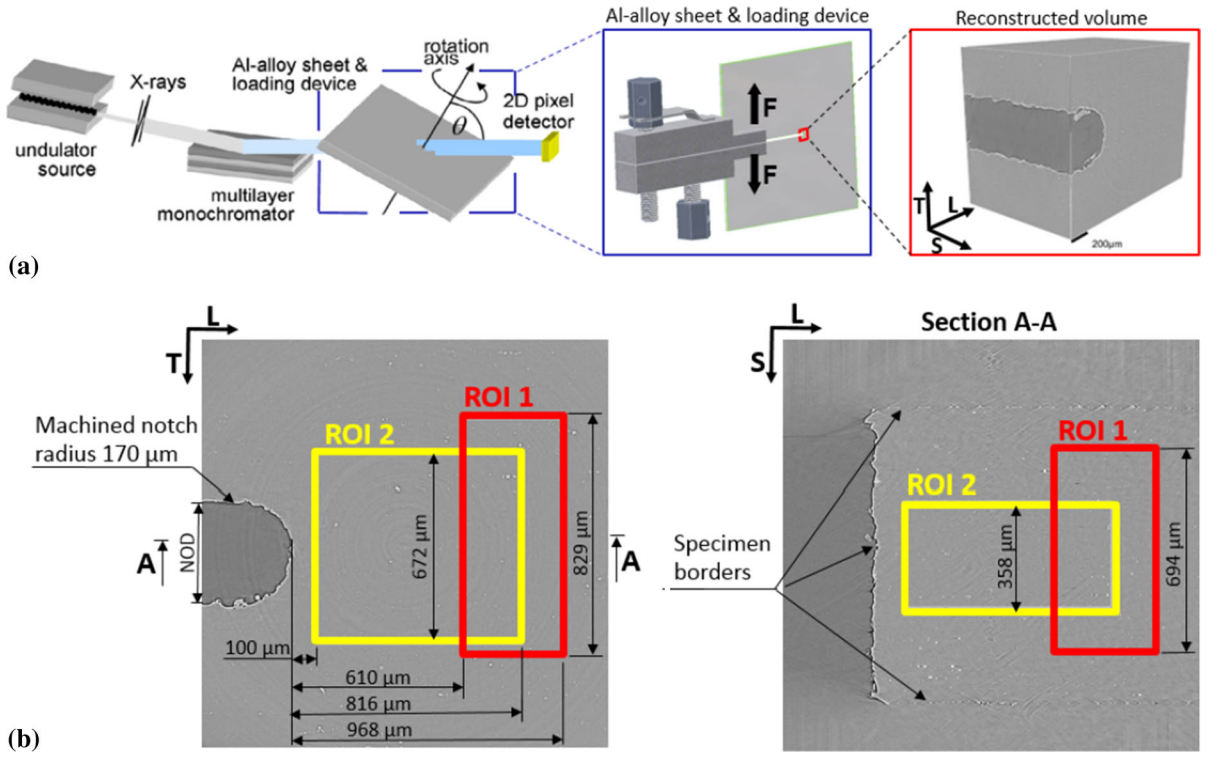

Fig. 3 (From Buljac et al. 2016). **a** Schematic view of the laminography experimental setup with scanned region in front of the notch root (*red*) and reconstructed volume. **b** Reconstructed volume sections with ROI positions and relevant dimensions for DVC analyses. ROI 1 corresponds to the analysis reported in Morgeneyer et al. (2014). The approximate notch opening displacement (NOD) measurement location is shown (initial value $2\,\rho = 340\,\mu$m has to be subtracted)

Table 1 Applied NOD measured on laminography images for loading steps 1 to 5 and at unstable fracture (Morgeneyer et al. 2014)

Load step	0	1	2	3	4	5	Failure
NOD (µm)	0	56	101	127	177	210	245
Time (s)	0	277	386	436	517	564	609

The corresponding time values are obtained with the FE analyses in Sect. 4

bands appear at plus and minus 45° with "hot spots" at band intersections. The band pattern is not symmetric with respect to mid-height (notch plane) and mid-thickness. These features are preserved for steps 2–3 and 3–4 but strain is more and more localized in the main band region. The band activity is highly variable but the bands locations do not change much, perhaps due to the large load steps.

The spacing between the bands ranges from 100 to 300 µm. By contrast, the strain heterogeneities that appear in the DIC images of the tensile specimens tested at $10^{-2}\,s^{-1}$, $10^{-3}\,s^{-1}$ and $10^{-4}\,s^{-1}$ are separated by more than 1 mm (the specimen width is 6 mm). The length scale of the strain heterogeneities seems to depend on the specimen geometry.

With the hypothesis of a one minute duration for each load step, the maximum strain rate in the bands increases approximately from $5 \times 10^{-4}\,s^{-1}$ in steps 1–2 and 2–3 to $10^{-3}\,s^{-1}$ in steps 3–4 (Fig. 4a). Outside the bands, the strain is still increasing in steps 1–2 and 2–3, with an approximate rate of $2 \times 10^{-4}\,s^{-1}$ (Morgeneyer et al. 2014; Buljac et al. 2016). In the case of damage-related strain localization, the strain rate contrast between the band and the adjacent material

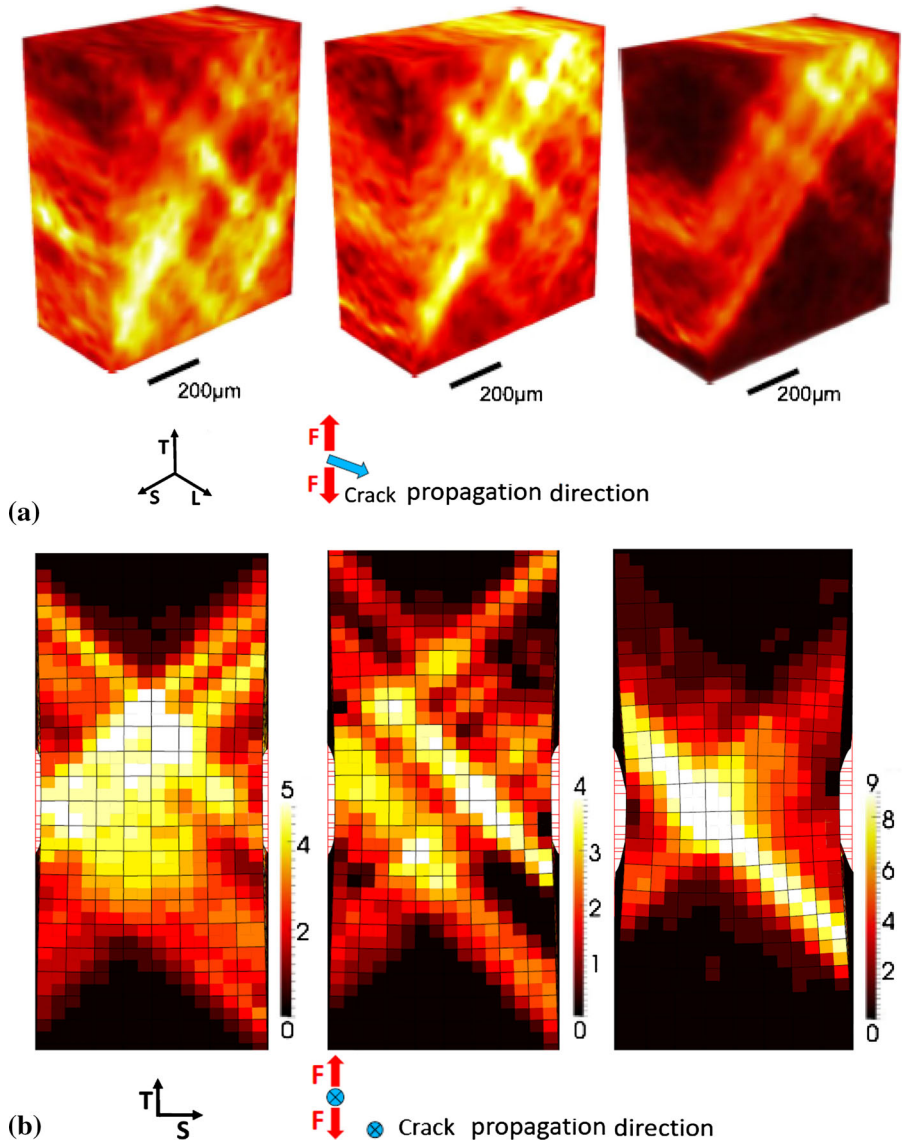

Fig. 4 *Incremental* von Mises equivalent strain fields: **a** DVC results in the ROI 1 (reduced thickness 0.694 mm), front L-section at x = 36.968 mm, undeformed geometry (from Morgeneyer et al. 2014), **b** FE analysis with the fine mesh, L-section x = 37 mm viewed from x+, full thickness 1 mm, deformed geometry, the initial mesh is in *red lines*. *From left to right*: loading steps 1–2, 2–3 and 3–4 (3–4* for FE analysis, stopped at NOD = 171 instead of 177 μm in Table 1). The scales in % are the same for DVC and FE

is expected to be larger. Moreover, damage could not be found at micrometer resolution (Morgeneyer et al. 2014). By contrast, a smaller incremental strain rate, approximately $10^{-4}\,s^{-1}$, is observed outside the bands in the right figures for steps 3–4; it corresponds to the localization that will lead to the final slant fracture. With the hypothesis of 5 s duration for each load step, probably closer to the real one, the strain rates still lie in the range 10^{-2} to $10^{-4}\,s^{-1}$.

Note that for steps 1–2–3–4 of Table 1, the damage is very small in ROI 1 (Morgeneyer et al. 2014). In the simulations (Sect. 4.5, fine mesh), the crack tip is at 0.06–0.2–0.3–0.8 mm from the notch tip, respectively. The front section of ROI 1 at 0.968 mm is not yet reached by the crack.

Figure 5a reveals the traces of the incremental strain bands in S-sections parallel to the specimen faces. (Incremental strain fields calculated by FE analysis are shown for comparison. They are discussed in Sect. 4.4.) Depending on the section (only mid-thickness sections are shown here) and on the loading step, one, two or three bands can be seen. A more quantitative assessment is given in Fig. 8 of Buljac et al. (2016). In their paper, it is also shown that at distances larger than ~250 μm from the notch tip, the strain in the crack propagation direction L is very small and deformation

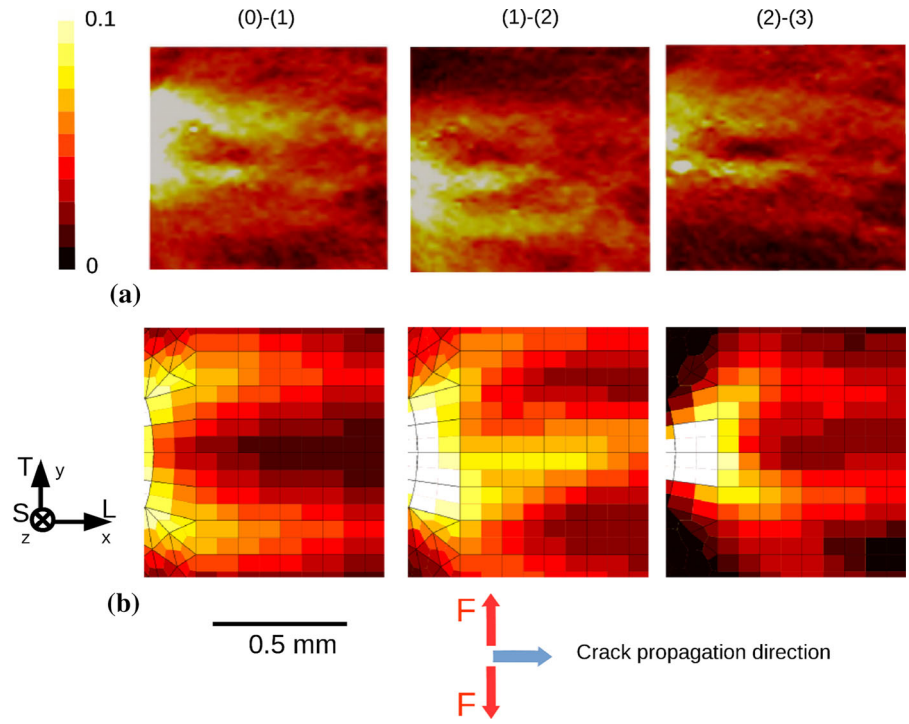

Fig. 5 *Incremental* von Mises equivalent strain fields, ROI 2, mid-thickness S-sections (z = 0), undeformed geometry with the notch on the *left*: **a** DVC analyses (from Buljac et al. 2016), **b** FE analysis with the fine mesh. *From left to right* loading steps 0–1, 1–2 and 2–3. The scale 0–0.1 is the same for DVC and FE

is mainly shear in the T–S plane. It can be concluded again that the band activity is highly variable but that the band locations do not change much; they are fixed by the presence of the notch.

2.4 Fracture results

The fracture surface scanning electronic microscopy (SEM) images of Fig. 6 show a typical flat-to-slant crack transition in a thin sheet made of the same material teared in similar conditions as in Morgeneyer et al. (2014). The crack initiates at the notch tip or very close to it and it first propagates in the notch plane in a flat triangular region. At a small distance from the notch, two shear lips form at the specimen surfaces. They join each other after ∼1 mm propagation and the crack becomes fully slanted. Large dimples corresponding to the intermetallic particles can only be seen in the flat triangular crack Fig. 6, but they are mixed with flat zones without visible dimples. The shear lips and slant zones could correspond to transgranular fracture. Similar fracture zones without dimples were already observed with SEM on the same alloy in the slanted cracks of Kahn and M(T) specimens (Chen 2011).

In Fig. 12 of Buljac et al. (2016), the overlay of L-section strain fields and final crack path reconstructed images shows that, at distances larger than ∼250 μm from the notch tip, the "flat" crack triangle actually is made of "zigzagged" failure patterns at the locations of the very early strain bands. Associated with the limited void damage, it supports the occurrence of an additional shear transgranular fracture mechanism in some aluminum alloys.

These features are confirmed in Fig. 7a, b showing the final damage ahead of the notch. In Fig. 7a, the reconstructed image of the damage (in blue) shows mainly the flat crack, together with some transgranular damage in the elongated grains in the L-direction (perpendicular to the notch round tip). In Fig. 7b, damaged zones are selected at a smaller scale. The slant crack appears at some distance from the notch (the elevation of each point is represented by a color scale). In the reconstructed S-sections of Fig. 7c, transgranular cracking is more visible than void damage; a small shear crack can be seen at the notch tip, corresponding to the additional fracture mechanism.

In Fig. 10 of Morgeneyer et al. (2014), 3D rendering of the very small initial porosity and of the void/damage

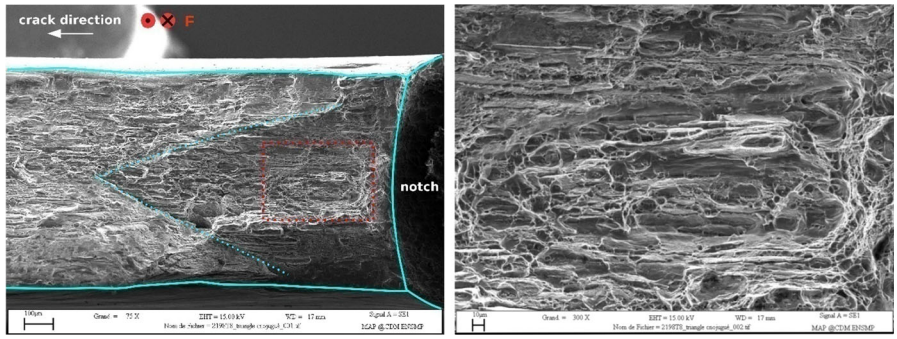

Fig. 6 SEM of the full thickness fracture surface (*left*, triangular flat zone) and of the flat zone (*right*, enlargement of the *red quadrangle in left figure*). The *horizontal bars* represent 100 and 10 μm, respectively

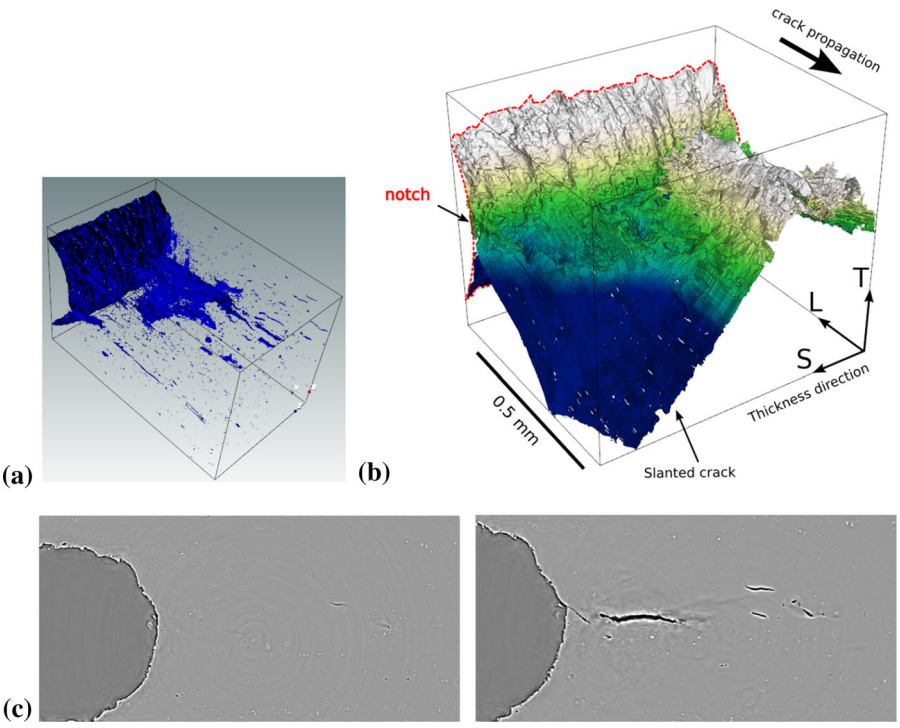

Fig. 7 Voids/cracks at the notch: **a** 3D rendering of damage in the laminography images investigated by DVC, **b** height map of the final crack, **c** 2D slices of reconstructed laminography data at mid-thickness normal to the S-direction for steps 4 (*left*) and 5 (*right*)

shows no evolution in ROI 1 after the first and second loading steps. Some damage appears for steps 3 and 4 but only in the regions of strain localization and the void volume fraction is still very limited (Fig. 8a). Final failure is characterized by a burst of localized damage forming a slanted crack (Fig. 8b). The slanted crack is very straight and seems to be transgranular. No damage can be seen after failure in the vicinity of the slanted crack. The nanometric dimples on the slant fracture surface are much smaller than the intermetallic particles (Fig. 8c). Slant strain localization is the critical event and nanometric voids only appear in the localization band after a large amount of deformation. Similar tomography results without dimples were obtained by Chen (2011) in the slanted cracks of Kahn specimens made of the same alloy.

3 Models

The results of Sect. 2 reveal two original features: (i) plastic deformation is heterogeneous at the macroscopic scale with the early formation of several intermittent shear strain bands ahead of the notch, (ii) ductile fracture mechanisms in the CT specimen are not only void nucleation, growth and coalescence but also transgranular fracture with limited diffuse damage development. Prior calculations using von Mises plasticity or

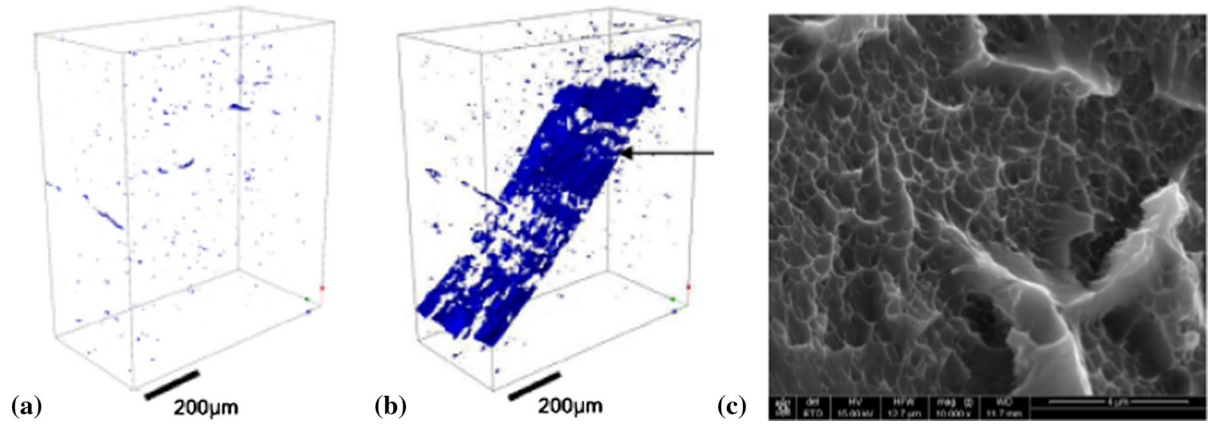

Fig. 8 Voids/crack in the ROI 1: **a, b** laminography images investigated by DVC for step 4 and after unstable fracture, respectively, **c** SEM of the slant fracture surface showing nanometric dimples, the *horizontal bar* represents 4 µm (Morgeneyer et al. 2014)

the GTN porous plasticity and ductile fracture model did not capture localization bands neither slant fracture (Morgeneyer et al. 2014; Ren et al. 2016). This indicated that plasticity modeling need to be enhanced to be able to capture the experimental findings in simulations. To make an attempt to improve the plasticity model and associated simulations, a well-known dynamic strain aging (DSA) model (Kubin and Estrin 1985; McCormick 1988; Kubin and Estrin 1990; Estrin and McCormick 1991; McCormick and Ling 1995; Zhang et al. 2001) is used in the present analyses. This so-called KEMC model is formulated here *at the slip system scale* (Rousselier and Quilici 2015). In addition, to account for fracture mechanisms not related to void damage, the Coulomb fracture model *at the slip system scale* (Rousselier and Luo 2014) is combined with porous plasticity (Rousselier 1981). It is emphasized that these combined models are all necessary to match the numerous experimental observations, as detailed in Sect. 4.1. The quantitative agreement is the result of parameter calibration, Sect. 4.2.

3.1 Plasticity

A polycrystalline plasticity model is the backbone of the present work. The framework of physically based polycrystalline metal plasticity has intrinsic advantages in describing the anisotropy and distortion of the yield surface, as well as realistic anisotropic hardening. Moreover, crystal plasticity is required to introduce the DSA and Coulomb models at the slip system scale. Besides, void nucleation and growth models have to be reformulated in the polycrystalline framework. A particular self-consistent polycrystalline model (Cailletaud 1992) was improved to model with accuracy the anisotropic behavior at large strain (Luo and Rousselier 2014). For brevity, only key ingredients of the polycrystalline plasticity model are presented here.

The polycrystal is composed of N grains (single crystals) that differ only by their crystallographic orientation. The single crystal model relates the slip rate $\dot{\gamma}_s$ and the resolved shear stress τ_s of each slip system ($s = 1$ to M, $M = 12$ for the FCC aluminum alloy). A phenomenological viscoplastic model (Cailletaud 1992) is used as the constitutive equations for each slip system:

$$\dot{\gamma}_s = \dot{v}_s Sign\left(\tau_s - X_s\right), \tag{1}$$

$$\dot{v}_s = |\dot{\gamma}_s| = Max\left[0, \left(\frac{|\tau_s - X_s| - r_s}{K}\right)^n\right], \tag{2}$$

$$r_s = r_s(v_s, v_t), \quad \forall t \neq s, \tag{3}$$

$$\dot{\alpha}_s = \dot{\gamma}_s - d\alpha_s \dot{v}_s, \quad X_s = c\alpha_s. \tag{4}$$

For each slip system, two scalar internal variables are introduced: $r_s = r_s(v_s, v_t)$ for isotropic hardening, depending on the *cumulated slips* v of the M slip systems, and α_s for kinematic hardening. Equation (4) defines a nonlinear kinematic hardening model (Armstrong and Frederick 1966; Chaboche 1977) with two parameters c and d. Viscoplastic flow reaches the rate-independent limit for large n and small K. Two constant hardening matrices H and K are introduced in the isotropic hardening equation:

$$r_s = R + Q_1 \sum_{t=1}^{M} H_{st} \left[1 - \exp\left(-b_1 v_t\right)\right] + Q_2 \sum_{t=1}^{M} K_{st} \left[1 - \exp\left(-b_2 v_t\right)\right]. \quad (5)$$

In Eq. (5), R is the initial critical resolved shear stress (CRSS) and the two hardening terms Q_1 and Q_2 depend on the cumulated slips of the M slip systems (self and latent hardening) through the two hardening matrices H and K. More details are given in Luo and Rousselier (2014). The 12×12 symmetric hardening matrices only depend on six parameters h_1 to h_6 and k_1 to k_6, respectively. Readers are referred to Rousselier et al. (2009) for the detailed elements of H (they are the same in K).

To establish a unique relationship between the stresses at the macroscopic and microscopic (i.e. crystal) scales, the so-called "β-rule" generalized for anisotropic materials is used (Cailletaud 1992; Sai et al. 2006). It requires a scalar modulus C of initial elastic accommodation close to the elastic shear modulus $\mu = E/(1+\nu)/2$, in accordance with Kröner's theory (Kröner 1971) and a fourth-order tensor of orthotropic anisotropy $\underline{\underline{D}}$. With the Voigt notation for the symmetric second-order tensors, $\underline{\underline{D}}$ has 10 independent elements D_{ij}.

3.2 DSA modeling

The physical origin of PLC is DSA, the pinning of dislocations by solute atoms that diffuse during straining. The dislocations are temporarily arrested at obstacles such as forest dislocations. Stress softening due to dislocation unpinning could be the cause of strain localization. It is postulated that each slip system has its own history of dislocation pinning and unpinning by solute atoms, corresponding to different aging times (Rousselier and Quilici 2015). For the KEMC model, the DSA term is added to the hardening Eq. (5) of each slip system (to shorten the equation, H and K are substituted with H_1 and H_2):

$$r_s = R + \sum_{i=1}^{2} Q_i \sum_{t=1}^{M} H_i^{st} \left[1 - \exp(-b_i v_t)\right] + P_1 \left[1 - \exp\left(-P_2 v_s^{\alpha} (t_a)_s^{\beta}\right)\right]. \quad (6)$$

The cumulated equivalent strain in the KEMC model is substituted here with the cumulated slip v_s of each slip system. P_1 and P_2 are multiplicative constants, α and β are exponents. The DSA term mainly depends on the aging time variables t_a (one for each slip system s), the rate equation of which is:

$$\dot{t}_a = 1 - \frac{|\dot{\gamma}|}{\omega} t_a. \quad (7)$$

3.3 Ductile fracture

Contrary to the GTN model, the Rousselier model: (i) fulfills the necessary kinematic condition for flat or slant macroscopic localization (Rousselier and Quilici 2015), (ii) has the ability to model ductile fracture in shear, (iii) can be reformulated in the polycrystalline framework (Rousselier and Leclercq 2006) with the plastic potential:

$$F = \frac{\sigma_{eq}}{1-f} - \left(\sum_{g=1}^{N} f_g \underline{\sigma}_g\right)_{eq} + D_1 f \sigma_1 \exp\left(\frac{\sigma_m^*}{(1-f)\sigma_1}\right), \quad (8)$$

In Eq. (8), σ_{eq} is the macroscopic von Mises equivalent stress, f is the void volume fraction, the grains of the matrix material $g = 1$ to N have the volume fractions $(1-f) f_g$ and the stress tensors $\underline{\sigma}_g$ (the equation for $\underline{\sigma}_g$ is not recalled here). D_1 and σ_1 are constants. As proposed in Morgeneyer et al. (2009), the mean macroscopic stress σ_m is substituted with σ_m^* to model 3D anisotropic void growth in an orthotropic material (principal axes of orthotropy: L, T, N). For isotropic void growth, $\alpha_L = \alpha_T = \alpha_N = 1/3$ and $\sigma_m^* = \sigma_m$:

$$\sigma_m^* = \alpha_L \sigma_{LL} + \alpha_T \sigma_{TT} + \alpha_N \sigma_{NN} \text{ with } \alpha_L + \alpha_T + \alpha_N = 1. \quad (9)$$

The void volume fraction rate is the sum of a first term due to the mass conservation law and a second term for void nucleation; $\dot{\varepsilon}_{eq}^p$ is the macroscopic von Mises equivalent strain rate:

$$\dot{f} = (1-f)\dot{\varepsilon}_{eq}^p D_1 f \exp\left(\frac{\sigma_m^*}{(1-f)\sigma_1}\right) + A\dot{\varepsilon}_{eq}^p. \quad (10)$$

In this paper, the factor A is a Gaussian function of the cumulated equivalent plastic strain ε_{eq}^p with parameters f_N, σ_N and ε_N (Chu and Needleman 1980):

$$A = \frac{f_N}{\sigma_N \sqrt{2\pi}} \exp\left[-\left(\frac{\varepsilon_{eq}^p - \varepsilon_N}{\sigma_N \sqrt{2}}\right)^2\right]. \quad (11)$$

For the Coulomb fracture model at the slip system scale, an additional slip rate $\dot{\gamma}_s^C$ activated at large strains is added to the slip rate $\dot{\gamma}_s$ of Eq. (1). The total slip rate is: $\dot{\gamma}_s^{tot} = \dot{\gamma}_s + \dot{\gamma}_s^C$. For $|\tau| + c_0\sigma_n \geq R_0$, the Coulomb slip γ_s^C and cumulated Coulomb slip are given by the viscoplastic rate equations:

$$\dot{\gamma}^C = Max\left[0, \left(\frac{|\tau| + c_0\sigma_n - R_0 \exp\left(-b_0\gamma_{cum}^C\right)}{K}\right)^n\right] Sign(\tau),$$
$$\dot{\gamma}_{cum}^C = \dot{\gamma}^C Sign\,(\tau)\,. \tag{12}$$

In Eq. (12), the index s of the slip system is not written. At the slip system scale, the only two stress components are the resolved shear stress τ and the normal stress σ_n. The Coulomb model depends on the two parameters R_0 and c_0. The novel feature in Eq. (12) is a slow decrease (small parameter b_0) of the critical stress with γ_{cum}^C, resulting in stress softening and strain localization.

To sum up, the macroscopic plastic strain rate tensor is:

$$\underline{\dot{\varepsilon}}^p = (1-f)\sum_{g=1}^{N} f_g \sum_{s=1}^{M} \underline{m}_{sg}\left(\dot{\gamma}_s + \dot{\gamma}_s^C\right) + f\frac{D_1}{3}\exp\left(\frac{\sigma_m^*}{(1-f)\sigma_1}\right)\dot{\varepsilon}_{eq}^p \underline{1}. \tag{13}$$

In Eq. (13), $\underline{m}_{sg}$ is the orientation matrix of each slip system; $\underline{1}$ is the unity matrix; $\dot{\varepsilon}_{eq}^p$ is calculated by taking the second invariant of the first right-hand term. The second right-hand term of Eq. (13) is the volumetric strain rate, obtained by derivation of the porous plastic potential Eq. (8); the DSA model is included in $\dot{\gamma}_s$; the Coulomb fracture model corresponds to $\dot{\gamma}_s^C$.

4 Finite element analyses

4.1 Objectives, constraints, limitations

As mentioned at the beginning of Sect. 3, the objective of finite element analyses in this paper is to model the particular features of plastic deformation and slant ductile fracture of the 2198-T8R CT specimen. As far as possible, the constitutive models are based on physical mechanisms and provide a quantitative agreement with the available experimental data.

In ductile fracture, a large amount of plastic deformation is involved. Therefore, a suitable modeling of large strain plasticity is a prerequisite for the analysis of the CT specimen. Moreover, both crack initiation at the notch tip and crack propagation generate highly non-proportional loading paths. At large strains and in non-proportional loading, the complex distortion of the yield locus is related to the activation and cross-hardening of different slip systems, depending on crystallographic orientations. Advanced macroscopic models give a good description of the initial plastic behavior of most metallic materials, in particular of initial anisotropy. However, the modeling of anisotropic hardening still is a difficult task for these models. By contrast, anisotropic hardening and non-proportional loadings are well captured using self-consistent polycrystalline plasticity, physically-based at the slip system scale.

A first constraint is the computation time in the numerical integration of the polycrystalline constitutive model. An accurate modeling of the material texture requires at least hundreds crystallographic orientations and thousands internal variables. Fortunately, a promising modeling of a large database of mechanical tests can be obtained with a significant reduction of the number of representative crystallographic orientations (Luo and Rousselier 2014). Usually, $N/4 = 3$ texture components and $N = 12$ orientations are sufficient for an initially orthotropic metal. This so-called reduced texture methodology (RTM) consists in applying a specific calibration procedure. The reduced texture parameters ($3N/4$ Euler angles and $N/4 - 1$ volume fractions) are calibrated with the mechanical tests only (Rousselier et al. 2009, 2010). It can be verified a posteriori that the reduced texture matches the real texture. A limitation of the present work is that tensile tests in 3 directions only were available to calibrate the model. Although the reduced texture is not accurately representative of the material, it is expected that the intrinsic qualities of the polycrystalline model are preserved. Another limitation is that crystallographic texture evolution is not modeled, although a few total slips $\gamma_s^{tot} = \gamma_s + \gamma_s^C$ can be very large near fracture.

In Kok et al. (2003), a DSA model was already introduced at the slip system scale in a polycrystalline model (using a Taylor-type assumption) for FE simulations of Al–2.5%Mg tensile specimens. The N-crystal aggregates assigned to the integration points have random orientations, with $N = 1$, 8 or 16 (same orientations in a given finite element). The objective is to introduce material heterogeneity with a length scale equal to the

element size when $N = 1$ and smaller when $N = 8$ or 16. It generates stress gradients and enables to model the complex spatio-temporal dynamics of jerky flow. In our simulations, the material is homogeneous and the length scale that spontaneously appears in the strain band patterns seems to be more related to the specimen geometry and size. Moreover, the KEMC model is more advanced than the "crude" one used in Kok et al.

To model crack initiation and propagation, it is also necessary to use ductile fracture models. In its broadest sense, ductile damage may be defined as the cause of failure processes involving a significant amount of dissipation. Various mechanisms can be involved (adiabatic softening at high strain rates and creep fracture mechanisms at high temperature are not considered in this paper):

1. plastic deformation diffuse macroscopic localization, like necking in round tensile specimens or in thin sheets,
2. shear fracture due to micro-shear bands localization at the slip system scale,
3. dimple fracture due to micro-voids initiation, growth and coalescence.

The first item is modeled provided the plasticity model is accurate enough. In aluminum alloys, no dimples are observed on some fracture surfaces, for example in AA6260 notched tension and shear specimens (Rousselier and Luo 2014). In the present AA2198 alloy, dimples are observed in the flat fracture zone only and even in this zone they are mixed with transgranular fracture surfaces without dimples. Therefore, the mechanism #2 can be involved. A specific model is required. The Coulomb fracture model at the slip system scale was used with success in Rousselier and Luo (2014). It is based on the resolved shear and normal stresses on the slip plane. Alternatively, a model based on a critical cumulated slip associated with a stress softening equation could be used, similar to the maximum shear strain model of Kim and Yoon (2015). In the analyses, the Coulomb fracture model competes with the porous plasticity model for the mechanism #3. Because of the very low initial porosity and the early intermetallic particle damage of the present alloy (Morgeneyer et al. 2014), a void *nucleation* model also is necessary.

4.2 Model parameters

The combined models of Sect. 4.1 involve a large number of parameters. The lack of appropriate number and kind of mechanical tests made it impossible to calibrate the initial anisotropy and the parameters of the KEMC model for the present material. Realistic values or parameters taken from the existing literature are used. By contrast, the experimental data enables a good calibration of the fracture parameters.

6260 and the present 2198-T8 aluminum alloys have the same small anisotropy of the tensile stress–strain curves in the sheet plane. That is why the available reduced texture parameters of AA6260 with $N = 12$ crystallographic orientations are used (Luo and Rousselier 2014). The calibration of the reduced texture (11 parameters for $N = 12$) would need at least additional tensile tests and shear tests in the sheet plane. For the same reason, the two hardening matrices terms are supposed to be all equal to one: $h_i \equiv 1$ and $k_i \equiv 1$. Because of the small positive strain rate effect of aluminum alloys at room temperature, the viscosity parameters n and K of Eqs. (2) and (12) are chosen to give a small effect of the viscoplastic stress $K\dot{\gamma}^{1/n}$ for a large range of shear rates $\dot{\gamma}$. The "β-rule" matrix is supposed to be isotropic with equal diagonal terms D_{ii} and zero non-diagonal terms D_{ij}. The remaining hardening parameters are the first seven ones in Table 2: from R to d. These parameters are calibrated with the tensile curve in the T-direction (single finite element calculation, Fig. 9). An optimization software is used with the Levenberg–Marquardt algorithm (Levenberg 1944). Because no tension-compression test was available, the kinematic hardening parameters c and d of Eq. (4) are calibrated like a third isotropic hardening term at large strain (exponent coefficient d smaller than b_1 and b_2). These two parameters are not representative of the real kinematic hardening of the material. Note that in Luo and Rousselier (2014), initial values of the back resolved shear stresses (kinematic hardening) at the slip system scale were implemented to model the small deviation from orthotropy resulting in tension-compression asymmetry (the so-called differential stress effect) and distinct shear curves in the two diagonal directions of the sheet plane. These values are equal to zero here.

In the calibration with the tensile test, the ductile damage parameters have a negligible effect: no significant damage softening can be seen in Fig. 9. The

Table 2 Hardening, viscosity, localization and elasticity parameters

R (MPa)	Q_1 (MPa)	b_1	Q_2 (MPa)	b_2	c (MPa)	d	h_i
101.0	23.9	6.41	9.9	3.51	49.3	1.065	1
k_i	n	K (MPa s$^{1/n}$)	D_{ii} (MPa)	D_{ij} (MPa)	C (MPa)	E (MPa)	ν
1	25	20	200	0	20,000	74,000	0.3

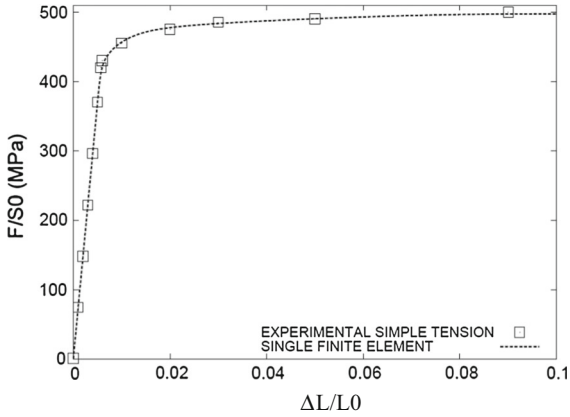

Fig. 9 Tensile curve in T-direction: F/S0 (MPa) versus ΔL/L0, experimental points and calibrated model curve. The maximum ΔL/L0 = 0.1 is applied in 100 s

dislocations are pinned because a large value $\omega = 0.04$ of the DSA strain parameter in Eq. (7) has been used, giving large waiting times $t_w = \omega/|\dot{\gamma}|$. In that case, the calibrated initial CRSS is $R + P_1$, i.e. 181 MPa for $P_1 = 80$ MPa. The values of P_1 in the polycrystalline model are larger than the ones in a macroscopic model because unpinning only impacts simultaneously a small fraction of the model $N \times M = 144$ slip systems. Experimental data were not designed to calibrate the DSA model. The three DSA parameters $P_2 = 4\text{s}^{-\beta}, \alpha = 0.1, \beta = 0.33$ in Table 3 are taken from the literature for aluminum alloys (Estrin and McCormick 1991; Graff et al. 2004; Benallal et al. 2008; Böhlke et al. 2009). In these papers, $\omega = 10^{-4}$ is used.

According to Eq. (6), the PLC domain approximately corresponds to $0 < t_a < 1$ s; see also Fig. 12a in Rousselier and Quilici (2015) obtained with $R + P_1 = 69$ MPa and $P_1 = 30$ MPa (same ratio R/P_1 as for the present alloy). The asymptotic value $t_a = t_w = \omega/|\dot{\gamma}|$ of Eq. (7) decreases when strain rate increases with plastic deformation and t_a decreases abruptly when

Table 3 KEMC model parameters

P_1 (MPa)	$P_2(\text{s}^{-\beta})$	α	β	ω
80	4	0.1	0.33	0.002

it crosses this value. Therefore, for slip rates in the order of $10^{-3}\,\text{s}^{-1}$, the PLC domain can be obtained for $\omega < 0.001$, approximately. In aluminum alloys, it corresponds to the PLC domain lower limit in strain rate and to the upper limit in temperature. For smaller values of P_1, at the same strain rates, t_a and ω have to be decreased simultaneously. The CT specimen has been calculated mainly with $P_1 = 80$ MPa. In that case, $\omega = 0.002$ is the smallest value for which the calculation does not diverge early (it diverges for $\omega = 0.0015$). Other couples (P_1, ω) have also been investigated ("Appendix 1").

The fracture parameters are given in Table 4. The rather flat tensile curve enables to define a flow stress σ_Y and the porous plasticity parameter $\sigma_1 = 2\sigma_Y/3 = 350$ MPa. $D_1 = 2$ is the value given by early void growth measurements (Rousselier 1987). The measured intermetallic particles volume fraction and initial porosity give f_N and f_0. Because of the very small initial porosity volume fraction, the mean nucleation strain $\varepsilon_N = 0.1$ is the decisive parameter; this value is representative of the intermetallic particles and it matches well the experimental crack growth. Nucleation is concentrated around this mean value with a small scatter $\sigma_N = 0.02$. Without experimental data for anisotropic void growth, $\alpha_L = \alpha_T = \alpha_N = 1/3$ is retained.

In this paper, we only use the Coulomb model with $c_0 = 0$, because the single fracture experiment does not enable to calibrate this parameter and also because the computational cost is reduced with a fully associated model (the Coulomb model with $c_0 \neq 0$ is non associated). The experimental balance between dim-

Table 4 Coulomb fracture model and porous plasticity parameters

D_1	σ_1 (MPa)	f_0	f_N	ε_N	ε_N slant	σ_N	f_c
2	350	0.0001	0.0034	0.1	0.05	0.02	0.15
c_0	R_0 (MPa)	R_0 slant (MPa)	b_0	γ_c^C	α_L	α_T	α_N
0	260	240	2	2	0.3333	0.3333	0.3333

ples and transgranular fracture in the triangular flat zone is obtained with $R_0 = 260$ MPa. To deal with the mesh orientation effect in local approach to ductile fracture, smaller values for $R_0 = 240$ MPa and $\varepsilon_N = 0.05$ are used in the shear lips and in the slant fracture zones defined in Sect. 4.3 (refer to this section and to Sect. 4.5 for a more complete discussion and reference to similar methods). These values for R_0 are calibrated to match the experimental crack growth. Although it is reduced to 0.05, the nucleation parameter ε_N has no significant effect in these zones because void damage is very small (Fig. 6).

The material is considered as "broken" when the void volume fraction exceeds some critical value: $f > f_c$ or when a first cumulated Coulomb slip exceeds some critical value: $\gamma_{cum}^C > \gamma_c^C$. A quadratic cumulative rule $(f/f_c)^2 + (\max(\gamma_{cum}^C)/\gamma_c^C)^2 = 1$ is used when porous plasticity and the Coulomb fracture model are combined. The material behavior is then replaced by an elastic behavior with a very low stiffness (Young's modulus $E_c = 1$ MPa). Gauss integration points where this condition is met are referred to as "broken Gauss points" (Morgeneyer et al. 2009). It is shown in Fig. 11 of Rousselier and Luo (2014) that displacements at failure of a notched tensile specimen differ by <1% with parameters in the ranges $0.15 < f_c < 0.25$ and $2 < \gamma_c^C < 3$. At these large values: $f = f_c = 0.15$ and $\max(\gamma_{cum}^C) = \gamma_c^C = 2$, the material has lost its mechanical strength because of almost complete stress softening, see for example Eq. (12) with $b_0 = 2$. Consequently, these two parameters have very little effect on the results and we must emphasize that *they are not fracture parameters* (contrary for example to f_c in the GTN model). They do not participate in strain localization. Their single function is to alleviate the calculation.

At the FE mesh level, when $nc = 4$ Gauss points of a reduced integration quadratic hexahedral element C3D20R (for example) are "broken", the element is removed from the calculation. It is not realistic to remove an element when only $nc = 3$ Gauss points out of the total number $n = 8$ are broken. It has been checked theoretically and with FE analyses that the removal criterion with $nc \geq 5$ gives no element deletion: with 4 out of 8 broken Gauss points, C3D20R elements have lost their load carrying capacity. That is why in some figures of Sect. 4.5 unbroken Gauss points (in white) are visible in the cracked areas, mixed with red broken points.

In conclusion, the only decisive parameters that could not be calibrated with experimental and literature data are the PLC parameters P_1 and ω.

4.3 Meshes

The element numbers are 13,000 and 29,360 in the coarse and fine meshes, respectively (Fig. 10). The Cartesian grid in the notch region, Fig. 10b, d, is designed with equal size C3D20R hexahedral elements to prevent the well-known "mesh size effect" in local approach to fracture. For the coarse mesh, the element size in the notch region is $0.25 \times 0.20 \times 0.25\,\text{mm}^3$ (four elements in the 1 mm thickness, z direction). For the fine mesh, it is $0.125 \times 0.10 \times 0.125\,\text{mm}^3$ (eight elements in the thickness). The elements are smaller in the y-direction to account for their elongation in the deformed state. For the same mesh size effect prevention, a special design is chosen at the notch tip, so that the element height in the deformed state is as close as possible to that of the Cartesian mesh, Fig. 10c, e. The design is completed with C3D15R prismatic elements. The Cartesian mesh is 2 mm long; it enables approximately 2 mm crack propagation with limited mesh size effect. The coarse and fine meshes are used to quantify the mesh size effect. With the fine mesh and the unstable DSA model, the calculations are very long; the coarse mesh also enables preliminary calculations at a reasonable cost. An accurate calculation of the mechanical fields can only be obtained with the fine

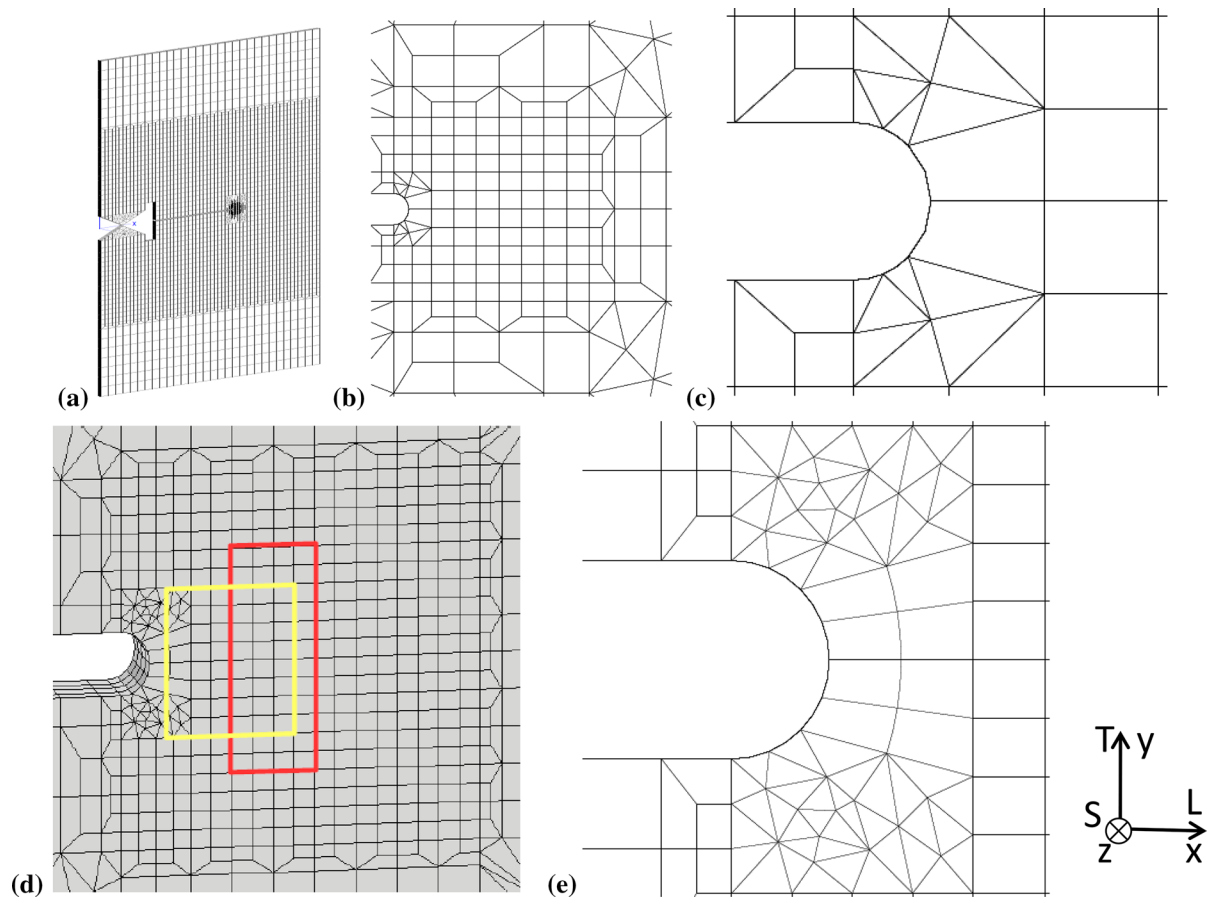

Fig. 10 3D meshes: **a–c** coarse mesh, four elements through the thickness; **d, e** fine mesh, eight elements through the thickness. Meshes **a** and **d** are tilted. In **d**, the positions of ROI 1 (*red*) and ROI 2 (*yellow*) are shown (at mid-thickness section, half geometry). The coordinates of the notch tip are x = 36 mm, y = 0

mesh, remember the ∼100–300 μm experimental band spacing in Figs. 4 and 5.

Displacements Uy and –Uy are imposed to the upper and lower rigid elastic triangles attached to the crack in Fig. 10a (Young modulus 10^7 MPa). The applied rate is 10^{-3} mm/s and the final value is Uy = 1 mm (Uy = time/1000). To prevent rigid-body motion, the point x = W = 60 mm, y = z = 0 (mid-height, mid-thickness) is fixed. To prevent buckling and mode III crack loading, Uz = 0 is imposed to the specimen mid-thickness z = 0, except a large zone surrounding the notch tip ($30 < x < 50$, $-5 < y < 5$). Without this kind of condition, buckling is effectively observed.

The NOD is calculated from the vertical displacements of mid-thickness nodes at 301 μm (coarse mesh) and 292 μm (fine mesh) from the notch tip (radius 170 μm). The NOD determined at 200 μm from the notch tip is smaller by less than 5 μm. The NOD is used in the comparisons with experimental observations, because the variable "time" does not correspond to the real loading history and because the load is not measured during the tests. (For that reason, the numerical load–displacement curves of Sect. 4.4 could not be compared to the experimental one.) In Table 1, the correspondence between NOD and time is obtained with the coarse mesh. It depends on numerical crack propagation. With the fine mesh, crack propagation is earlier and the time values are slightly different.

It has been shown, for example in Rousselier and Quilici (2015) with the same models, that crack propagation is much more rapid in one of the Cartesian

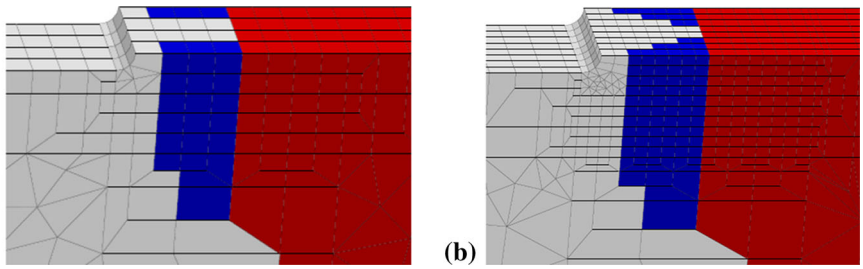

Fig. 11 Slant region (*red*) and shear lip region (*blue*), half meshes, sections y = 0, notch on the *left*: **a** coarse mesh and **b** fine mesh

mesh directions than at 45° of it. It is the "mesh orientation effect" in local approach to fracture. It can be prevented with the so-called non-local models (Forest and Lorentz 2004; Bargellini et al. 2009; Feld-Payet et al. 2011; Bergheau et al. 2014). These models increase the computational cost and they are beyond the scope of the present work. A more pragmatic way is to use different fracture parameters in the flat fracture region on the one hand and in the shear lips and slant fracture regions on the other hand ($R_0 = 260$ and 240 MPa in Table 4, respectively). These regions are known *a priori* from the SEM fractographies of Fig. 6. This approach is not entirely predictive but it is effective in the present case. The regions are defined in Fig. 11.

The method used in Morgeneyer and Besson (2011) is not so different. The authors have introduced an additional strain-based void nucleation model with a Lode angle dependence that promotes shear fracture. Consequently, this ad-hoc model gives the shear lips. The two lips eventually join at mid-thickness, forming slant fracture. Instead of different parameters for the same models in the present work, the authors use different models in the flat and slanted fracture zones. This method is not convenient here because there is no void nucleation in the shear lips and slant fracture regions. In Chen (2011), the Cartesian mesh of a Kahn specimen is gradually slanted to follow the experimental flat-to-slant transition, successively avoiding the mesh orientation effect. As the two preceding ones, this third method is not entirely predictive.

An order-2 Runge–Kutta algorithm with automatic time stepping is used for the material model. The tangent matrix is the elastic one. The finite strain formulation is based on the so-called co-rotational frame associated with the rotation tensor (e.g. Rousselier and Luo 2014, Appendix 1). The equilibrium is solved with a Newton–Raphson algorithm.

4.4 Load serrations and PLC bands

According to Table 1, the applied NOD rate increases from 0.2 to 0.8 μm/s. In Fig. 4b, the numerical strain rate is between 5×10^{-4} and $2 \times 10^{-3}\,s^{-1}$ for load steps 1–2, 2–3 and 3–4, with time increments ∼100, 50 and 50 s, respectively. The experimental load steps are applied in less than 10 s, i.e. the stain rate is larger, but still in the PLC range 10^{-4} to $10^{-2}\,s^{-1}$ (Sect. 2).

In the load–displacement curves of Fig. 12, a small scatter can be seen for several runs of the same configuration (coarse or fine mesh), even with the same single processor and therefore the same rounding errors correction algorithm, because of the unstable characteristic of the DSA model, Eq. (7). The different results are probably seeded by the random exchanges between the two cores used in the calculations or by the random share between several users of the processor. Load inflexions appear in Fig. 12 for Uy ∼ 0.300 mm (time = Uy/1000 ∼ 300 s). Before this displacement, there is no difference between the coarse and fine mesh curves because damage is small and it is limited to a very small zone at the notch tip. The first broken Gauss point and the first removed element appear in the two fine mesh calculations at time = 250–250 and 301–311 s, respectively. In the five coarse mesh calculations, the time ranges of these two events are 295–300 and 454–467 s, respectively. Classically, crack growth is more rapid in the fine mesh which results in a lower load curve and slightly delayed load oscillations. (The first removed element appears much later in the coarse mesh also because two layers of elements are involved in flat fracture vs. a single layer in the fine mesh, see Sect. 4.5. Thus, by contrast with the broken point events, the removed element events are not mechanically relevant.)

The large sinusoidal oscillations of Fig. 12 are not commonly observed in experimental load–displacement curves. The maximum time increment $\Delta t = 1$ s can be too large to capture well the instabilities generated by

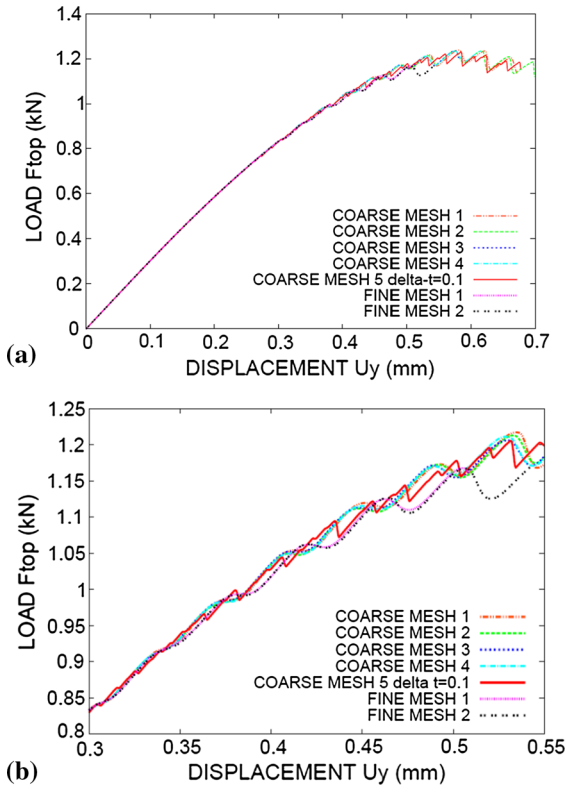

Fig. 12 Load (kN) versus displacement curves: **a** Uy range 0–0.7 mm, **b** Uy range 0.3–0.55 mm. The MESH numbers correspond to several calculations with the same coarse or fine meshes and with the same material parameters $P1 = 80$ MPa and $\omega = 0.002$. The maximum time increment is $\Delta t = 1$ s, except for COARSE MESH 5 ($\Delta t = 0.1$ s)

the DSA model (the automatic time stepping algorithm is not activated by the DSA model in the present calculations). With $\Delta t = 0.1$ s (COARSE MESH 5), the red curve shows more realistic serrations. For example, the load decreases for Uy = 0.3046 to 0.3064 mm. This range exactly corresponds to the appearance and disappearance of strain rate bands ahead of the notch. The same correspondence is observed for the following load decreases. In this #5 calculation, the broken Gauss points appear at the notch tip in the intervals Uy = 0.2981–0.3062 mm (4 points), 0.3800–0.3812 mm (+4 points), 0.4063–0.4079 mm (+6 points), etc. They form two layers of broken integration points on each side of the symmetry plane y = 0. The broken point events always fall in the load decrease events but with $\Delta t = 0.1$ s the latter are much more numerous in the range Uy = 0.3–0.45 mm. For Uy > 0.475 mm, load decreases, strain rate bursts and broken points always coincide. It shows that the intermittent PLC bands and the broken point events are strongly related. PLC may well be the initiator of broken point events.

The coarse mesh calculations with $\Delta t = 1$ and 0.1 s give very close crack propagation rates. Both give crack growth during strain rate band bursts. The difference is that for $\Delta t = 1$ s these events are much longer and consequently the load oscillations are much larger.

Smaller values $P_1 = 40$ and 30 MPa have been investigated using the coarse mesh, with $\omega = 0.0005$–0.0003 and 0.0001, respectively. The results are given in "Appendix 1". In the rest of this Sect. 4, we only consider $P_1 = 80$ MPa and $\omega = 0.002$ for both coarse and fine meshes with the maximum time step $\Delta t = 1$ s.

The strain rate bands are better visible with the fine mesh. The occurrence of 2 or 3 horizontal bands on the specimen surface is emphasized in Fig. 13. The figures are slightly tilted around the y axis (positive rotation angle) to show the notch tip inner surface on the left. The strain rate is zero at mid-thickness in the notch tip because the Gauss points are broken, but the small flat crack does not yet extend to the surfaces (similar to the left inset in Fig. 18, "Appendix 1"). At time = 385 and 425 s (Uy = 0.385 and 0.425 mm), the successive strain rate bursts are clearly shown, both on specimen surface and through the thickness (section AA at 1 mm from the notch tip). As in the coarse mesh, they coincide with discontinuous crack propagation steps: no broken integration points for time = 350–376 s, 14 additional broken points for time = 377–393, no broken points for time = 394–417, etc. At time = 425 s, the crack forms a flat triangle shorter than 0.4 mm, it shows that the strong interaction between strain rate and crack propagation bursts begins in the flat fracture regime. The load has two minima at time = 385 and 430 s, in accordance with the strain rate bursts of Fig. 13.

The calculated incremental strain fields (FINE MESH 1) are compared to the measured ones in Fig. 4 of Sect. 2.3. The full thickness (1 mm) is shown because the small number of Gauss integration points cannot be reduced without an important loss of information. The deformed mesh is used to evidence the small displacements of the incremental bands, which seem to be immobile in the DVC figures. In the latter, the ROI 1 thickness only is ~0.7 mm and the initial geometry is used. The large load increments 1–2, 2–3 and 3–4 encompass several load oscillations with slightly different locations of the calculated strain rate bands, which

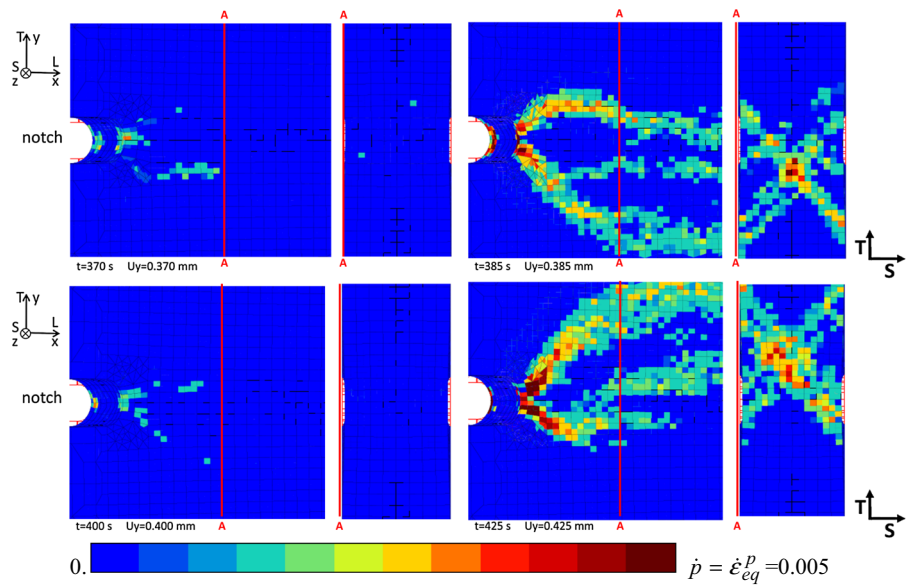

Fig. 13 Strain rate fields, fine MESH 1 calculation, front surface z = +0.5 mm tilted mesh (Cartesian mesh region, 0–2 mm from the notch) with the notch on the left and section AA at Δx = 1 mm from the notch (view from x+) for time = 370–385–400–425 s. The strain rate range is 0–0.005 s^{-1}, *navy blue* to *dark red*). The initial meshes are in *red lines*

could explain this difference. Nevertheless, the same experimental method was applied to another aluminum alloy with much smaller load steps and no significant band motion was detected (Morgeneyer et al. 2016). The large PLC amplitude P_1 in the analyses could also increase the band motion.

Apart from the band mobility, which is slightly larger in the numerical simulations, there are strong similarities between the band patterns: several parallel bands at plus and minus 45° with "hot spots" at band intersections, no symmetry with respect to mid-height (y = 0) and mid-thickness (z = 0), similar strain levels although there are no "black zones" (very small values) in the two left DVC figures. The hot spots correspond to distinct micro-mechanical mechanisms, as evidenced in the infrared thermography measurements of Delpueyo et al. (2016), and to distinct slip systems in the numerical analyses, which accumulate at the crossing points. The inter-band spacing of several hundred microns cannot be related to crystallographic heterogeneities. It strongly suggests that DSA is the cause of multiple banding. Anyway, DSA is not a completely deterministic phenomenon and a strictly identical band pattern was not expected. For steps 3–4, the localization in a single band is more advanced in the calculation, probably because with the fine mesh the crack is larger than the experimental one, see Sect. 4.5. When the crack approaches the section x = 37 mm of Fig. 4, the crack geometry imposes a single band, flat or slanted depending on the specimen geometry (the thickness in particular that impacts the mechanical fields) and on the parameters of the various fracture mechanisms. Note that in Fig. 4b the numerical main band is at plus 45° in the yz plane, i.e. perpendicular to the experimental main band of Fig. 4a. Because of the random characteristic of the DSA model, the result plus or minus 45° depends on the calculation.

Figure 14 enables a more quantitative comparison. The cumulated equivalent strain in the main localization band is about twice as large as in the surrounding area for load steps (1), (2) and (3), in DVC as in FE analysis. For load step (4), the ratio is larger than 2 and the band is narrower for DVC. In FE analyses, the strain rate bands are more mobile than in the measurements and consequently the *total* cumulated strain is less localized. This early PLC-related strain localization is distinct from the late damage-related strain localization where plastic yielding takes place within the band only and the outer region undergoes elastic unloading. In the 2198-T8R alloy, the latter localization is linked to the former. This mechanism could be general for this class of aluminum alloys (Morgeneyer et al. 2016). By contrast with Fig. 4, the total strain for the whole history is shown in Fig. 14; that is why the main band only is clearly visible, particularly in the finite element calculation with slightly moving strain rate bands. Figure 14 also does not show the strain *rate* band mobility.

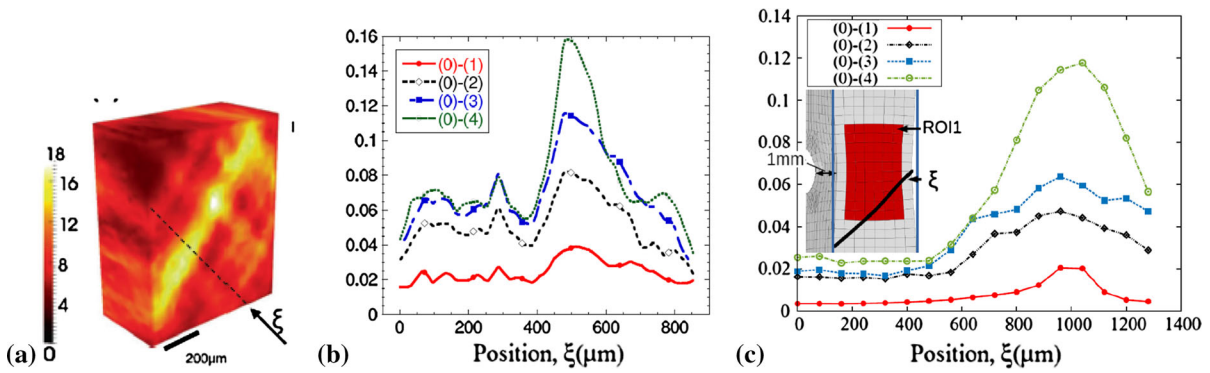

Fig. 14 Total cumulated von Mises equivalent strain along a line perpendicular to the localization band for load steps 1–4, deformed geometry for the abscissa ξ: **a, b** measured by DVC along line ξ in the plane at $\Delta x = 1$ mm from the notch (step 4 in Fig. 14a), initial reduced thickness 0.694 m (ROI 1), from Fig. 8 in Morgeneyer et al. (2014) and **c** fine MESH 1 calculation, initial full thickness 1 mm

4.5 Ductile fracture

The results for both coarse and fine meshes are presented. The DSA model parameters are $P_1 = 80$ MPa and $\omega = 0.002$. In Fig. 15, the damage variables are shown on the surface y = 0. The notch is on the right, the thickness S-direction is vertical. The flat crack and the intersection of the slant crack with the plane z = −0.5 mm can be seen in some figures (because of thickness reduction in Fig. 15c, d). The void volume fraction is large in the triangular flat fracture zone only: Fig. 15a, e for the coarse and fine meshes, respectively. It is negligible in the shear lips and in the slant crack although a smaller value for the void nucleation strain ε_N was used in these regions. It is not homogeneous because it competes with transgranular fracture, according to the SEM images of Fig. 6. As mentioned in Sect. 4.2, a good balance between dimples and transgranular fracture in the flat zone is obtained with the Coulomb critical resolved shear stress $R_0 = 260$ MPa. A few maps of the Coulomb slips are presented for both meshes. The critical Coulomb slip depends on the local stress and strain tensors; that is why several slip systems are involved in crack growth. Some of the ones with the larger Coulomb slips are shown in Fig. 15g. For example, at the notch tip, the critical Coulomb slip index is 85 (Fig. 15h) which means grain $g = 8$ and slip system $s = 1$ ($7 \times 12 + 1 = 85$); it corresponds to the normal to the slip plane {0.773, −0.599, 0.212} and slip direction {−0.440, −0.649, −0.227} (undeformed geometry values) that give a pure shear strain in a plane close to the xy plane, parallel to the specimen surface (the shear plane is the one formed by the first two eigenvectors of the orientation matrix $\underline{m}_{sg}$, they are close to the directions x and y). The crack initiates with this Coulomb slip, in agreement with the small shear crack in Fig. 7c and with the small stress triaxiality σ_m/σ_{eq} in the vicinity of the notch free surface that limits void damage. Void damage only prevails at some distance from the notch, Fig. 15e. Note that $\sigma_m/\sigma_{eq} \leq 1$ in the whole specimen. This small value for a CT specimen is due to the very small relative thickness B/W = 1/60. In the standard CT specimens with B/W = 25/60, maximum stress triaxiality is larger than 2.5. It partly explains the limited void damage in the experiment and the prevalence of the Coulomb model in the numerical analyses.

The damaged zones are smaller in the fine mesh figures because they correspond to a smaller applied NOD (the calculation incidentally stopped at NOD = 199 µm). This displacement corresponds to the ∼1 mm crack of Fig. 15j: the white integration points are broken (zero stress). The shear lips are already well developed; the front one can be seen on the specimen surface (the mesh is tilted). In the fine mesh, unbroken points are visible on the surfaces. The reason why was explained at the end of Sect. 4.2: only 4 broken points out of 8 integration points are possible in one element, some of them are hidden. This mixed pattern is not seen in the coarse mesh because the element thickness is twice larger in the perpendicular direction and the damage concentrates in two layers of integration points adjacent

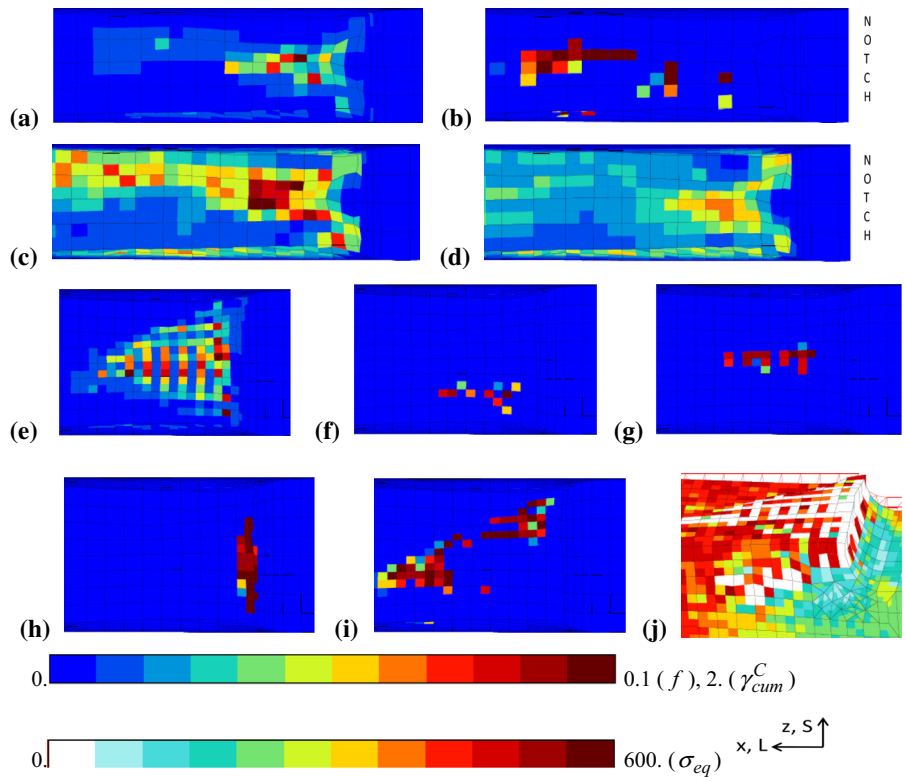

Fig. 15 **a–d** coarse MESH 2 calculation, lower half of the specimen y < 0, the notch is on the *right*, time = 698, NOD = 335 μm: **a** void volume fraction, scale 0–0.1, **b–d** Coulomb slips 99, 116, 126, respectively, scale 0–2. **e–j** fine MESH 2 calculation, upper half of the specimen y > 0, the notch is on the right, time = 542, NOD = 199 μm: **e** void volume fraction, scale 0–0.1, **f–i** Coulomb slips 13, 71, 85, 116, respectively, scale 0–2, **j** von Mises equivalent stress, scale 0–600, tilted mesh, the initial mesh is in *red lines*

to the plane y = 0 (Fig. 16a); the four broken points are all visible on this plane.

For the applied NOD = 242 μm, the coarse mesh L-sections of Fig. 16a give the experimental flat zone length of ∼1 mm. The right transition from flat to slant fracture is obtained with R_0 = 240 MPa (Table 4) in the shear lips and in the slant region of Fig. 11a. With R_0 = 245 MPa, slant fracture is delayed and the slant crack is not as nice as the one in Fig. 16b. With R_0 = 250 MPa, shear lips and slant fracture are not obtained. The transition from flat to slant fracture is also shown in Fig. 16c with the intersections of the crack and the surfaces y = 0 (mid-height) and z = −0.5 mm (specimen surface).

The three values R_0 = 240–245–250 MPa in the shear lips—slant crack regions have also been tested in the coarse mesh without DSA (ω = 0.020 instead of 0.002, that suppresses the load serrations and the strain rate bands). Slant fracture is obtained with R_0 = 240 and 245 MPa, not with R_0 = 250 MPa. Because of the completely pinned dislocations with ω = 0.020, the stresses and the load are slightly larger and consequently the Coulomb model gives earlier crack propagation than with ω = 0.002. By contrast, the load is smaller *after* crack initiation. Void damage is much smaller than the experimental one in the flat crack. Without DSA, slightly larger values of R_0 in *both* the flat crack and the shear lips—slant crack regions should be used to match physical damage and experimental crack path and growth rate.

The CT specimen has also been calculated with the same R_0 parameter in the whole mesh (coarse mesh). With R_0 = 260 MPa, the crack does not quit the direction of the Cartesian mesh, it remains flat. With R_0 = 250 MPa, a shear lip forms on one side of the specimen and after 2 mm propagation it encompasses only the half of the specimen thickness. With R_0 = 240 MPa, the flat crack stops too early, slant crack propagation is obtained but it is too rapid and the maximum load is much smaller. These results do not fit experimental data and observations. Two distinct values for the R_0 parameter are necessary in the present calculations.

Figure 17 is for the fine mesh. The MESH 1 and MESH 2 calculations incidentally stopped at time = 508 and 542 s, respectively (Fig. 12b). The flat crack terminates in L-section Δx = 0.875 mm from the notch tip. The deformed mesh shows that a

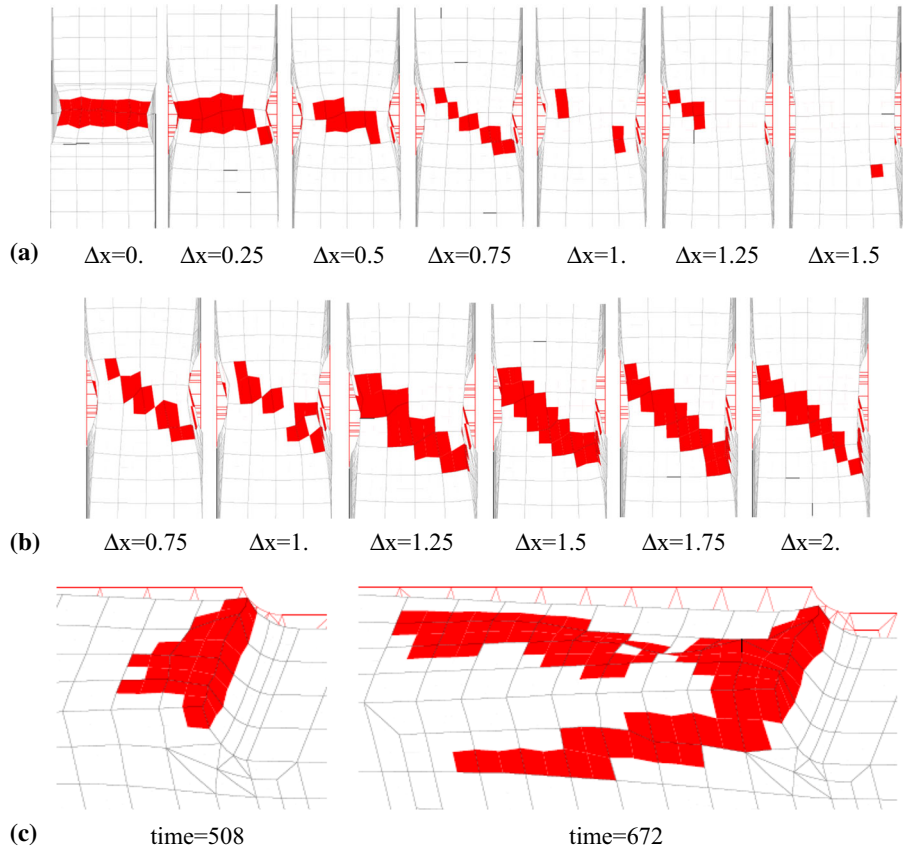

Fig. 16 Broken Gauss points. **a** Coarse MESH 2 calculation, time = 610, NOD = 242 μm, notch tip x = 36 mm (Δx = 0). Viewed from x = 0 and L-sections viewed from x+ at Δx = 0.25–0.50–0.75–1–1.25–1.50 mm from the notch. **b** Coarse MESH 2 calculation, time = 698, NOD = 335 μm, L-sections at Δx = 0.75–1–1.25–1.50–1.75–2 mm from the notch. **c** Coarse MESH 1 calculation, lower half of the specimen y < 0, tilted mesh with the notch on the *right*, time = 508 and 672, NOD = 171 and 302 μm respectively. The initial meshes are in *red lines*

single layer of finite elements is involved in flat fracture, with two discontinuous layers of broken points. The unbroken points in the removed elements make the "discontinuous crack artifact" not visible in the coarse mesh.

Figure 17b shows the intermittent crack growth in relation with the DSA model. The figures at time = 465 and 483 s correspond to the beginning and the end of a PLC band event and they show a large crack propagation causing a load decrease in Fig. 12. On the contrary, there is almost no crack propagation from time = 483–498 s, only one additional broken point can be seen in the shear lip. The next strain rate burst and intermittent crack growth occur at time = 500–520 s. In Fig. 17b, the broken point patterns are somewhat different for MESH 1 (time = 498) and MESH 2 (time = 542). As expected, the NOD increase rate is larger during the crack propagation periods. In the laminography experiments on the ductile 2139-T3 aluminum alloy (Morgeneyer et al. 2016), smaller load increments were applied to a CT specimen and experimental stepwise crack growth was observed, similar to the one in the present calculations.

5 Discussion

The laminography observations of a 2198-T8R aluminum alloy CT-like specimen revealed unexpected deformation patterns and early strain localization in slant bands in the slant fracture region (Morgeneyer et al. 2014). It was a challenge to simulate this experiment because the material database is limited and not designed for this purpose and because the calculations are at the limits of numerical capabilities. In the future, a new experimental program should include both laminography and a comprehensive characterization database. Moreover, the experimental results showed complex interactions between plastic behavior and ductile fracture. Ductile fracture itself resulted from various mechanisms. The backbone of the present work is to contribute to the understanding of the het-

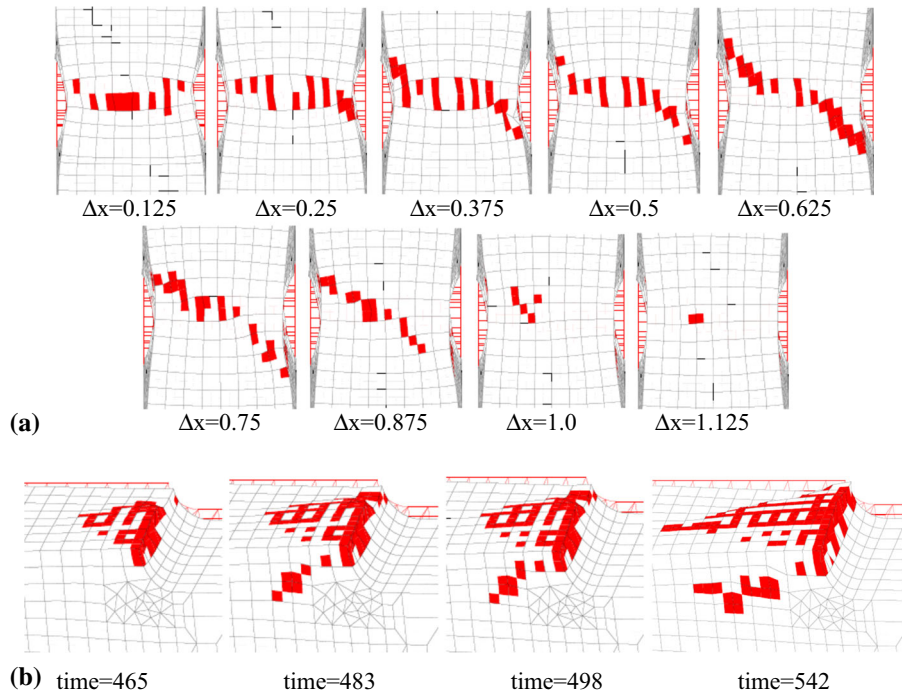

Fig. 17 Broken Gauss points, **a** fine MESH 2 calculation, time = 542, Uy = 0.542, NOD = 199 μm, L-sections at Δx = 0.125–0.25–0.375–0.5–0.625–0.75–0.875–1.0–1.125 mm from the notch, view from x+, **b** fine MESH 1 (time = 465–483–498, Uy = time/100, NOD = 142–160–163 μm respectively) and fine MESH 2 (time = 542, NOD = 199 μm) calculations, upper half of the specimen y > 0, tilted mesh with the notch on the *right*. The initial meshes are in *red lines*

erogeneous deformation ahead of the sharp notch using enhanced plasticity models.

First, the physical origin of the strain bands is not straightforward. On the one hand, the intermittent character of the bands seems to exclude the microstructural heterogeneity hypothesis. Also, the length scale, larger than 1 mm in tensile specimens (6 mm width) and smaller than 0.3 mm in the CT specimen (1 mm thickness), is not in favor of this hypothesis. Clearly, the length scale is related to the specimen geometry and dimensions and to the mechanical fields resulting from the boundary conditions. With infrared thermography measurements of 5052 aluminum-magnesium alloy tensile specimens loaded at strain rates larger than 10^{-2} s^{-1}, Delpueyo et al. (2016) observed moving and intermittent band patterns similar to the ones in the present CT specimen but with a ∼5 mm length scale related to the large 40 mm width of the specimens.

On the other hand, the 2198-T8R alloy is at the limit of the PLC domain in tensile tests at room temperature and for the usual constant strain rates considered in the present work. Also, the intermittent bands seem to be fixed ahead of the notch of the CT specimen, which is not usual for the PLC phenomenon. This could be explained by the physical origin of the PLC phenomenon: DSA first takes place inside the grains and because DSA is limited in this material and testing conditions, it could be hardly visible at the macroscopic scale in tensile tests. The strain heterogeneities could remain related to the grain microstructure and/or be seeded by it, which could explain the fixed bands in Figs. 4 and 5 and also the fixed strain localization patterns in a 2139-T3 aluminum alloy (Morgeneyer et al. 2016). This latter alloy has more work-hardening than AA2198-T8R and equiaxed grains (mean sizes 60–52–24 μm in the L–T–S directions), nevertheless the band spacing is the same in the CT specimen: 150–250 μm. This explanation would perhaps conciliate the "DSA" and "microstructural heterogeneity" points of views. The latter is modeled in Taupin et al. (2016): the enforcement of tangential continuity conditions of the distortion rate along grain boundaries spontaneously gives shear bands patterns in the L–S plane of AA2198 rolled sheets. Nevertheless, these patterns are different from the ones in Fig. 4.

For these aluminum alloys and this large in-plane dimensions CT specimen (W/B = 60), the plastic deformation is concentrated in a small region ahead of the notch. That is why, by contrast with smooth tensile specimens, the PLC phenomenon is not expected to give large serrations of the load–displacement curve. In the notch region, numerical simulations show a strong

interaction between PLC and flat or slant ductile fracture and consequently the load inflexions and oscillations are also due to crack initiation and propagation. The coarse mesh calculations with sufficiently small time steps $\Delta t = 0.1$ s give realistic load serrations (Figs. 12, 18). Unfortunately, a satisfactory modeling of the strain rate bands could only be obtained with the fine mesh and in that case only $\omega = 0.002$ and $\Delta t = 1$ s were within affordable computation times. The combination of small ω and large time steps gives early divergence of the calculation. (In the present work, the smallest ratio without divergence is $\Delta t/\omega = 500$ s for the applied loading rate. It corresponds approximately to $1 > \Delta t/t_w > 0.2$ with the waiting time $t_w = \omega/\dot{p}$ and the equivalent strain rate $2 \times 10^{-3}\,\mathrm{s}^{-1} < \dot{p} < 5 \times 10^{-4}\,\mathrm{s}^{-1}$ in the bands.)

Although the 2198-T8R alloy is at the limit of the PLC domain in classical tensile tests at room temperature and the KEMC model parameters were not calibrated with these tests, it does not really impact the results of this work. Actually, the stepwise loading of the CT specimen was performed with a screw system that results in relaxation between load steps. Recently, relaxation periods were shown to give PLC-type serrations and localization in tensile specimens made of 2139-T3 aluminum alloy although no PLC effect is observed in constant strain rate tests (Ren et al. 2017). Both the present KEMC model and the parameter calibration with constant strain rate tests can be questioned for complex loading paths (Böhlke et al. 2009). It was beyond the scope of this work to simulate the complex loading history of the CT specimen. The simulation results are to be considered in relation with laminography to support the role of DSA in the observed strain patterns.

Special care was given to the mesh design in order to limit mesh effects in ductile fracture modeling. Two mesh sizes are used to quantify the mesh size effect. Comparing Figs. 16a and 17a, it can be seen that in both meshes the thickness of the fracture process zone is equal to one element size in both flat and slant cracks, i.e. twice larger in the coarse mesh, which delays crack initiation and propagation. In the flat crack, there are two parallel layers of broken integration points in both meshes, but they are located differently, in one and two layers of finite elements for the fine and coarse meshes, respectively. These mesh effects could be eliminated with regularized models. They include non-local models or higher-order continua models. The combination of DSA and PLC modeling with strain gradient plasticity has been shown in various publications (Aifantis 1987; Hähner 1993; Mazière and Forest 2015; Mazière et al. 2016).

The two micro-mechanisms of ductile fracture are modeled with two distinct models: porous plasticity and Coulomb fracture model. These mechanisms do not correspond to flat and slant fracture. Dimples and transgranular fracture are both observed in the flat crack of Fig. 6 as well as in the slant fracture surface of a notched tensile specimen made of AA6260 (Rousselier and Luo 2014). The balance seems to be material dependent and the mechanisms should be carefully checked in ductile fracture experiments.

6 Conclusions

At room temperature, tensile tests on many aluminum alloys show evidence of dynamic strain aging (DSA), resulting in the Portevin–Le Chatelier (PLC) effect. It is the case for the Al–Cu–Li recrystallized 2198-T8R alloy that exhibits serrations on the tensile curves, an inverse strain effect, non-homogeneous strain rates in the gauge length of the tensile specimens and through-the-thickness slant fracture. On the tensile specimen surface, digital image correlation (DIC) does not reveal mobile inclined strain rate bands, contrary to some other aluminum thin sheets. Large compact tension (CT) specimens were also tested with high-resolution in situ synchrotron X-ray laminography combined with digital volume correlation (DVC) to measure the plastic strain fields and the damage ahead of the crack-like notch. The main experimental observations are several parallel inclined strain bands at $\pm 45°$ in L-sections perpendicular to the crack plane, flat to slant fracture transition without micrometric dimples in the shear lips and in the slant crack and no damage outside the slant crack (Morgeneyer et al. 2014).

These observations suggest some interaction between PLC and fracture for this thin aluminum sheet. To further investigate this point, finite element analyses of the CT specimen have been performed. Prior calculations using von Mises plasticity or the GTN porous plasticity and ductile fracture model did not capture the localization bands neither slant fracture (Morgeneyer et al. 2014; Ren et al. 2016). Contrary to the GTN model, the Rousselier model fulfills the necessary kinematic condition for flat or slant macroscopic localiza-

tion and it has the ability to model ductile fracture in shear (Rousselier and Quilici 2015). Moreover, it can be reformulated in the framework of polycrystalline plasticity. This model is combined with the Chu and Needleman (1980) model for void nucleation and with the Coulomb fracture model formulated *at the slip system scale* to account for transgranular fracture mechanisms not related to void damage. The Kubin–Estrin–McCormick (KEMC) model *at the slip system scale* is used for DSA. The main conclusions are:

- Although the fracture models involve many material parameters, most of them can be determined with the available material data. The main remaining parameters are the mean strain ε_N for void initiation and the Coulomb critical shear stress R_0. They are calibrated to match stable crack growth before final failure and the balance between void-related and void-free ductile fracture mechanisms. To account for the mesh orientation effect, different values are used for the flat fracture region and for the shear lips and slant fracture regions.
- The PLC parameters are taken from the literature for aluminum alloys, except the stress amplitude $P_1 = 80$ MPa and the time parameter $\omega = 0.002$. For $P_1 = 0$ or for a large value $\omega = 0.020$ (pinned dislocations), DSA is not activated; the load–displacement curve displays neither serrations nor oscillations. Nevertheless, slant fracture is obtained with the calibrated Coulomb stress $R_0 = 260$–240 MPa (flat-slant). For a quantitative and qualitative modeling, DSA activation with $\omega \leq 0.005$ is necessary. For this material, the combination of all the above-mentioned models is required to match the whole set of experimental measurements and observations.
- For $P_1 = 80$ MPa and $0.002 \leq \omega \leq 0.005$, bursts of strain rate bands are obtained, corresponding to the decreasing part of the load oscillations or serrations. Crack growth takes place during these time periods. Strain rates could not be determined experimentally because of the small number of loading steps in laminography, but the measured incremental strain fields between successive steps are in good agreement with the numerical incremental strain fields. If DSA is not activated, multiple bands cannot be obtained.
- This early PLC-related strain localization is distinct from the late damage-related strain localization where plastic yielding takes place within the band and the outer region is plastically inactive. In the present 2198-T8R alloy, the latter is linked to the former. This mechanism could be general for this kind of materials. Nevertheless, the numerical strain rate bands are slightly moving whereas the experimental ones seem to be fixed. The DSA activation could be related to some microstructural features. The microstructure alone cannot be the main origin of the bands because they are intermittent. Moreover, the inter-band spacing is well predicted with the DSA model.
- The increasing crack growth rates corresponding to the successive strain rate bursts could lead to "pop-ins" or even to unstable slant fracture like the one in the experiment, but this result could not be achieved in the present calculations because of numerical divergence for $\omega \leq 0.0015 (P_1 = 80$ MPa) or too large computation times for $P_1 < 80$ MPa ($\omega \leq 0.0003$).

The numerical analyses have important limitations:

- Mechanical tests were not available to calibrate the anisotropic plasticity model (reduced crystallographic texture and mechanical parameters) and the PLC model. Nevertheless, the results support the interaction of PLC with both plasticity and ductile fracture for this material.
- Numerical problems have not been addressed in the present work: (i) convergence accuracy, (ii) first stress invariant accuracy in relation with the volumetric plastic strain constraint (incompressibility or void growth), (iii) divergence and increasing computation times with decreasing PLC parameter ω and the related small time step Δt, (iv) mesh dependence (size, orientation, other characteristics). The mesh size effect has been observed with the coarse and fine meshes. The mesh orientation effect has been accounted for in a pragmatic way with two sets of fracture parameters R_0 and ε_N. The experimentally observed unstable slant fracture could probably be modeled with smaller values of ω as in Rousselier and Quilici (2015).

Future studies are required for a better understanding and modeling of the interaction between DSA and ductile fracture:

- The DSA model could be enhanced to account for non-monotonic loading.

- The numerical integration of the DSA model could be improved to reduce the computation time and to avoid early divergence.
- A numerically efficient method has to be developed for the unresolved problem of the mesh effect in the transition from flat to slant fracture.
- The PLC effect is temperature and loading history dependent. Future studies would better include these factors.
- DSA and ductile fracture are highly dependent on microstructure. The present modeling methodology could be applied to other aluminum alloys and heat treatments.
- For the present aluminum alloy, the existing Kahn tests could be used to calibrate the two parameters of the Coulomb fracture model (R_0 and c_0).

Appendix 1

Smaller values $P_1 = 40$ and 30 MPa have been investigated using the coarse mesh, with $\omega = 0.0005$–0.0003 and 0.0001, respectively (the calculations diverge early for smaller values of ω). The parameter R is increased from 101 to 141 and 151 MPa (same $R + P_1$), respectively, to account for the smaller PLC amplitudes P_1. Although they assume completely pinned dislocations, these corrections approximately give the same load levels in Fig. 18 up to Uy $\sim$ 0.580 mm. Therefore, the damage models (porous plasticity and mainly the Coulomb fracture criterion which is very sensitive to the stress level) are not much impacted and the crack growth is almost the same. Note that for $\omega = 0.0003$ and 0.0001 (pink and red curve), the maximum time step had to be reduced (from $\Delta t = 1$ s to $\Delta t = 0.1$ s) to catch the sharp variations of the aging time, Eq. (7). With this small time increment, the CPU time already is 24 days for the coarse mesh. (The clock time is 13.5 days with two cores. It is not significantly reduced with 4 or 8 cores.) Although the coarse mesh only gives poor images of the strain rate band patterns, fine mesh calculations have not been attempted with these small values of the ω parameter.

Small load decreases are obtained for $P_1 = 30$ MPa and $\omega = 0.0001$ (red curve in Fig. 18). For exam-

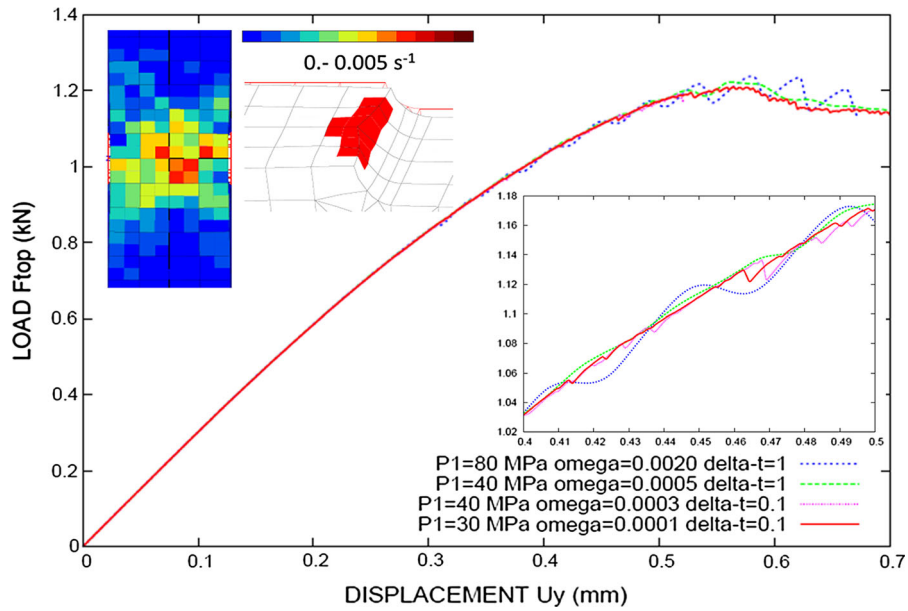

Fig. 18 Load (kN) versus displacement curves, effect of DSA parameters $P1$ and ω, coarse mesh. The maximum time increment is $\Delta t = 1$ s for $\omega = 0.0020$ and 0.0005, $\Delta t = 0.1$ s for $\omega = 0.0003$ and 0.0001. *Right insert* zoom with Uy range 0.4–0.5 mm (time = 400–500 s). *Left inserts* for the *red continuous curve* ($P_1 = 30$ MPa and $\omega = 0.0001$), (**i**) average equivalent strain rate for Uy range 0.4129–0.4139 mm (time = 412.9–413.9) in the L-section x = 37 mm (at $\Delta x = 1$ mm ahead of the notch, view from x+) and (**ii**) broken integration points (in *red*) for Uy = 0.4130 mm (time = 413), tilted mesh lower part $y < 0$, the notch is on the *right*, the initial meshes are in *red*

ple, the load decreases from 1.0551 to 1.0531 kN for Uy = 0.4129 to Uy = 0.4139 mm. Four or five crossing incremental PLC bands can be guessed in the L-section $x = 37$ mm, from Uy = 0.4115 to Uy = 0.4145 mm, although they are smeared by the coarse mesh (left inset in Fig. 18). The band pattern and spacing are similar to the ones in Fig. 13. In these bands, the von Mises equivalent strain rate in the 0.4129–0.4139 interval is approximately 0.004 s^{-1} in a few integration points of the L-section; it is about twice the average value in the full thickness. At Uy = 0.4127 and 0.4130 mm, two additional integration points are broken in the lower T-section $y < 0$ (left inset in Fig. 18), forming a small "triangular" crack with the prior six broken points at the notch tip. (The configuration is the same in the upper T-section $y > 0$.) There are no other "broken point events" in the large interval from Uy = 0.3878 to Uy = 0.4544 mm. It shows that the intermittent PLC bands and the broken point events are strongly related also for $P_1 = 30$ MPa and $\omega = 0.0001$. The load decreases because of simultaneous ductile damage (microvoids and/or microcracks, crack propagation) and DSA softening (dislocation unpinning) tentatively modeled by the porous plasticity, Coulomb fracture and KEMC models, respectively.

Appendix 2

In the J-Δa curve of Fig. 19, J is computed from the numerical load–displacement curve, according to ASTM1820 standard. Maximum crack growth length Δa_{max} is measured in the deformed geometry by taking the position of the farthest broken integration point in the fine mesh flat crack. The stepwise curve is due to the incremental crack propagation in FE simulations. The variation of J versus crack opening displacement (COD = 2 Uy = time/500) is also shown in Fig. 19. It can be noticed that the J-COD curve shows some oscillations after 0.6 mm. It corresponds to the oscillations in the load–displacement curve of Fig. 12. (These oscillations are not representative of the PLC effect because of the large maximum time step $\Delta t = 1$ s in the fine mesh simulations. Also, Δa_{max} is not representative of the complex crack growth shape that can be seen for example in Fig. 17b. The present numerical J-Δa curve is given for information purposes only.)

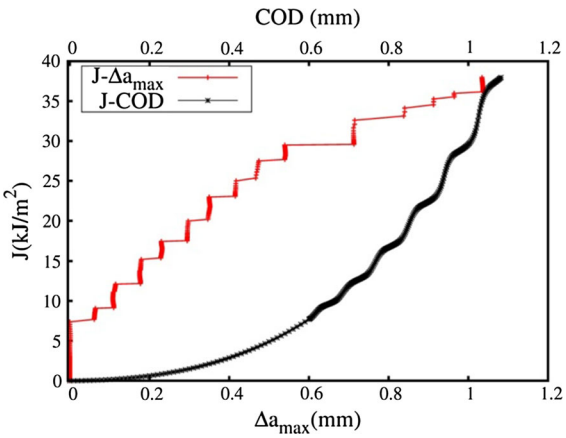

Fig. 19 Fine MESH 2 calculation, J versus Δa_max (*red curve*) and J versus COD (*black curve*)

References

Aifantis EC (1987) The physics of plastic deformation. Int J Plast 3:211–248

Armstrong PJ, Frederick CO (1966) A mathematical representation of the multiaxial Bauschinger effect. Report RD/B/N731, Central Electricity Generating Board, Berkeley, UK

Bargellini R, Besson J, Lorentz E, Michel-Ponnelle S (2009) A non-local finite element based on volumetric strain gradient: application to ductile fracture. Comput Mater Sci 45:762–767

Belotteau J, Berdin C, Forest S, Parrot A, Prioul C (2009) Mechanical behavior and crack tip plasticity of a strain aging sensitive steel. Mater Sci Eng A 526:156–165

Benallal A, Berstad T, Borvik T, Hopperstad O, Koutiri I, de Codes R (2008) An experimental and numerical investigation of the behavior of AA5083 aluminum alloy in presence of the Portevin–Le Chatelier effect. Int J Plast 24:1916–1945

Bergheau J-M, Leblond J-B, Perrin G (2014) A new numerical implementation of a second-gradient model for plastic porous solids, with an application to the simulation of ductile rupture tests. Comput Methods Appl Mech 268:105–125

Besson J (2010) Continuum models of ductile fracture: a review. Int J Damage Mech 19:3–52

Besson J, Steglich D, Brocks W (2001) Modeling of crack growth in round bars and plane strain specimens. Int J Solids Struct 38:8259–8284

Besson J, McCowan CN, Drexler ES (2013) Modeling flat to slant fracture transition using the computational cell methodology. Eng Fract Mech 104:80–95

Böhlke T, Bondar G, Estrin Y, Lebyodkin MA (2009) Geometrically non-linear modeling of the Portevin–Le Chatelier effect. Comput Mater Sci 44:1076–1088

Buljac A, Taillandier-Thomas T, Morgeneyer TF, Helfen L, Roux S, Hild F (2016) Slant strain band development during flat to slant crack transition in AA 2198 T8 sheet: in situ 3D measurements. Int J Fract 200:49–62

Cailletaud G (1992) A micromechanical approach to inelastic behavior of metals. Int J Plast 8:55–73

Chaboche JL (1977) Viscoplastic constitutive equations for the description of cyclic and anisotropic behavior of metals. Bull Acad Polon Sci Sér Sci Tech XXV 1:33–39

Chen JQ (2011) Ductile tearing of AA2198 aluminum–lithium sheets for aeronautic applications. Ph.D. thesis, Materials, Ecole Nationale Supérieure des Mines de Paris. <NNT: 2011 ENMP 0040>. <pastel-00657028>

Chu CC, Needleman A (1980) Void nucleation effects in biaxially stretched sheets. J Eng Mater Technol Trans ASME 102:249–256

Clausen AH, Borvik T, Hopperstad OS, Benallal A (2004) Flow and fracture characteristics of aluminum alloy AA5083-H116 as function of strain rate, temperature and triaxiality. Mater Sci Eng A 364:260–272

Coulomb CA (1773) Sur une application des règles de maximis et minimis à quelques problèmes de statique, relatifs à l'architecture. In: Théorie des machines simples, pp 318–363

Delafosse D, Lapasset G, Kubin LP (1993) Dynamic strain-aging and crack propagation in the 2091 Al–Li alloy. Scr Metall Mat 29:1379–1384

Delpueyo D, Balandraud X, Grédiac M (2016) Calorimetric signature of the Portevin–Le Chatelier effect in an aluminum alloy from infrared thermography measurements and heat source reconstruction. Mater Sci Eng A 651:135–145

El-Naaman SA, Nielsen KL (2013) Observations on Mode I ductile tearing in sheet metals. Eur J Mech A/Solids 42:54–62

Estrin Y, McCormick PG (1991) Modelling the transient flow behaviour of dynamic strain ageing materials. Acta Metall Mater 39:2977–2983

Feld-Payet S, Besson J, Feyel F (2011) Finite element analysis of damage in ductile structures using a nonlocal model combined with a three-field formulation. Int J Damage Mech 20:655–680

Forest S, Lorentz E (2004) Localization and regularization. In: Besson J (ed) Local approach to fracture. Ecole des Mines de Paris/Les Presses, pp 311–373

Graff S, Forest S, Strudel J-L, Prioul C, Pilvin P, Béchade J-L (2004) Strain localization phenomena associated with static and dynamic strain ageing in notched specimen: experiments and finite element simulations. Mater Sci Eng A 387:181–185

Hähner P (1993) Modeling the spatio-temporal aspects of the Portevin–Le Chatelier effect. Mater Sci Eng A 164:23–34

Helfen L, Morgeneyer TF, Xu F, Mavrogordato MN, Sinclair I, Schillinger B, Baumbach T (2012) Synchrotron and neutron laminography for three-dimensional imaging of devices and flat material specimens. Int J Mater Res 2:170–173

Kok S, Bharathi MS, Beaudoin AJ, Fressengeas C, Ananthakrishna G, Kubin LP, Lebyodkin M (2003) Spatial coupling in jerky flow using polycrystal plasticity. Acta Mater 51:3651–3662

Kim JB, Yoon JW (2015) Necking behavior of AA 6022–T4 based on the crystal plasticity and damage models. Int J Plast 73:3–23

Kröner E (1971) Zur plastischen Verformung des Vielkristalls. Acta Metall 9:155–161

Kubin LP, Estrin Y (1985) The Portevin–Le Chatelier effect in deformation with constant stress rate. Acta Metall 33:397–407

Kubin LP, Estrin Y (1990) Evolution of dislocation densities and the critical conditions for the Portevin–Le Chatelier effect. Acta Metall Mater 38:697–708

Lebyodkin M, Dunin-Barkowskii L, Brechet Y, Estrin Y, Kubin LP (2000) Spatio-temporal dynamics of the Portevin–Le Chatelier effect. Acta Mater 48:2529–2541

Le Chatelier A (1909) Influence du temps et de la température sur les essais au choc. Rev Métall 6:914–917

Le Jolu T, Morgeneyer TF, Denquin A, Sennour M, Laurent A, Besson J, Gourgues-Lorenzon A-F (2014) Microstructural characterization of internal welding defects and their effect on the plastic behavior of FSW joints of AA 2198Al–Cu–Li alloy. Metall Mater Trans A 45:5531–5544

Le Jolu T, Morgeneyer TF, Denquin A, Gourgues-Lorenzon A-F (2015) Fatigue lifetime and tearing resistance of AA2198 alloy friction stir welds: effect of defects. Int J Fatigue 70:463–472

Levenberg K (1944) A method for the solution of certain nonlinear problems in least squares. Q Appl Math 2:164–168

Luo M, Rousselier G (2014) Modeling of large strain multiaxial deformation of anisotropic metal sheets with strength-differential effect using a reduced texture methodology. Int J Plast 53:66–89

Mahgoub E, Deng X, Sutton MA (2003) Three dimensional stress and deformation fields around flat and slant cracks under remote mode I loading conditions. Eng Fract Mech 70:2527–2542

McCormick PG (1988) Theory of flow localization due to dynamic strain ageing. Acta Metall 36:3061–3067

McCormick PG, Ling CP (1995) Numerical modelling of the Portevin–Le Chatelier effect. Acta Metall Mater 43:1969–1977

Maire E, Withers PJ (2014) Quantitative X-ray tomography. Int Mat Rev 59(1):1–43

Maire E, Zhou S, Adrien J, Dimichiel M (2011) Damage quantification in aluminum alloys using in situ tensile tests in X-ray tomography. Eng Fract Mech 78:2679–2690

Marchenko A, Mazière M, Forest S, Strudel JL (2016) Crystal plasticity simulation of strain aging phenomena in alpha-titanium at room temperature. Int J Plast 85:1–33

Mazière M, Forest S (2015) Strain gradient plasticity modeling and finite element simulation of Lüders band formation and propagation. Continuum Mech Thermodyn 27:83–104

Mazière M, Besson J, Forest S, Tanguy B, Chalons H, Vogel F (2010) Numerical aspects in the finite element simulation of the Portevin–Le Chatelier effect. Comput Methods Appl Mech Eng 199:734–754

Mazière M, Luis C, Marais A, Forest S, Gaspérini MM (2016) Experimental and numerical analysis of the Lüders phenomenon in simple shear. Int J Solids Struct. doi:10.1016/j.ijsolstr.2016.07.026

Morgeneyer TF, Besson J (2011) Flat to slant ductile fracture transition: tomography examination and simulations using shear-controlled void nucleation. Scr Mater 65:1002–1005

Morgeneyer TF, Besson J, Proudhon H, Starink MJ, Sinclair I (2009) Experimental and numerical analysis of toughness anisotropy in AA2139 Al-alloy sheet. Acta Mater 57:3902–3915

Morgeneyer TF, Helfen L, Mubarak H, Hild F (2013) 3D digital volume correlation of synchrotron radiation laminography images of ductile crack initiation: an initial feasibility study. Exp Mech 53:543–556

Morgeneyer TF, Taillandier-Thomas T, Helfen L, Baumbach T, Sinclair I, Roux S, Hild F (2014) In situ 3-D observation of early strain localization during failure of thin Al alloy (2198) sheet. Acta Mater 69:78–91

Morgeneyer TF, Taillandier-Thomas T, Buljac A, Helfen L, Hild F (2016) On strain and damage interactions during tearing: 3D in situ measurements and simulations for a ductile alloy (AA2139-T3). J Mech Phys Solids 96:550–571

Nahshon K, Hutchinson JW (2008) Modification of the Gurson model for shear failure. Eur J Mech A/Solids 27:1–17

Papasidero J, Doquet V, Mohr D (2014) Determination of the effect of stress state on the onset of ductile fracture through tension–torsion experiments. Exp Mech 54(2):137–151

Pardoen T, Hutchinson JW (2003) Micromechanics-based model for trends in toughness of ductile metals. Acta Mater 51:133–148

Portevin A, Le Chatelier F (1923) Sur le phénomène observé lors de l'essai de traction d'alliages en cours de transformation. C R Acad Sci Paris 176:507–510

Ren SC, Rousselier G, Morgeneyer TF, Mazière M, Forest S (2016) Numerical investigation of dynamic strain ageing and slant ductile fracture in a notched specimen and comparison with synchrotron tomography 3D-DVC. Procedia structural integrity. Elsevier, 21st European conference on fracture, ECF21, 20–24 June 2016, Catania, Italy, vol 2, pp 3385–3392

Ren SC, Morgeneyer TF, Mazière M, Forest S, Rousselier G (2017) Portevin–Le Chatelier effect triggered by complex loading paths in 2139T3 aluminum alloy. Submitted for publication to Philosophical Magazine Letter

Rousselier G (1981) Finite deformation constitutive relations including ductile fracture damage. In: Nemat-Nasser S (ed) Three-dimensional constitutive relations and ductile fracture. North-Holland, Amsterdam, pp 319–343

Rousselier G (1987) Ductile fracture models and their potential in local approach of fracture. Nucl Eng Des 105:97–111

Rousselier G, Leclercq S (2006) A simplified polycrystalline model for viscoplastic and damage finite element analyses. Int J Plast 22:685–712

Rousselier G, Luo M (2014) A fully coupled void damage and Mohr–Coulomb based ductile fracture model in the framework of a reduced texture methodology. Int J Plast 55:1–24

Rousselier G, Quilici S (2015) Combining porous plasticity with Coulomb and Portevin–Le Chatelier models for ductile fracture analyses. Int J Plast 69:118–133

Rousselier G, Barlat F, Yoon JW (2009) A novel approach for anisotropic hardening modeling—part I: theory and its application to finite element analysis of deep drawing. Int J Plast 25:2383–2409

Rousselier G, Barlat F, Yoon JW (2010) A novel approach for anisotropic hardening modeling—part II: anisotropic hardening in proportional and non-proportional loadings, application to initially isotropic material. Int J Plast 26:1029–1049

Sai K, Cailletaud G, Forest S (2006) Micro-mechanical modeling of the inelastic behavior of directionally solidified materials. Mech Mater 38:203–217

Simonsen BC, Tornqvist R (2004) Experimental and numerical modelling of ductile crack propagation in large-scale shell structures. Mar Struct 17:1–27

Taupin V, Chevy J, Fressengeas C (2016) Effect of grain-to-grain interactions on shear strain localization in Al–Cu–Li rolled sheets. Int J Solids Stuct 000:1–11

Wang H, Berdin C, Mazière M, Forest S, Prioul C, Parrot A, Le Delliou P (2011) Portevin–Le Chatelier (PLC) instabilities and slant fracture in C–Mn steel round tensile specimens. Scr Mater 64:430–433

Zhang S, McCormick PG, Estrin Y (2001) The morphology of Portevin–Le Chatelier bands: finite element simulation for Al–Mg–Si. Acta Mater 49:1087–1094